Division of Synchrotron Radiation Science

X-ray Photoelectron Spectroscopy on Clusters: From Water Clusters to Metal & Metal-Oxide Nanoparticles

Emmanouil Tzomos
Master Thesis, Spring 2021
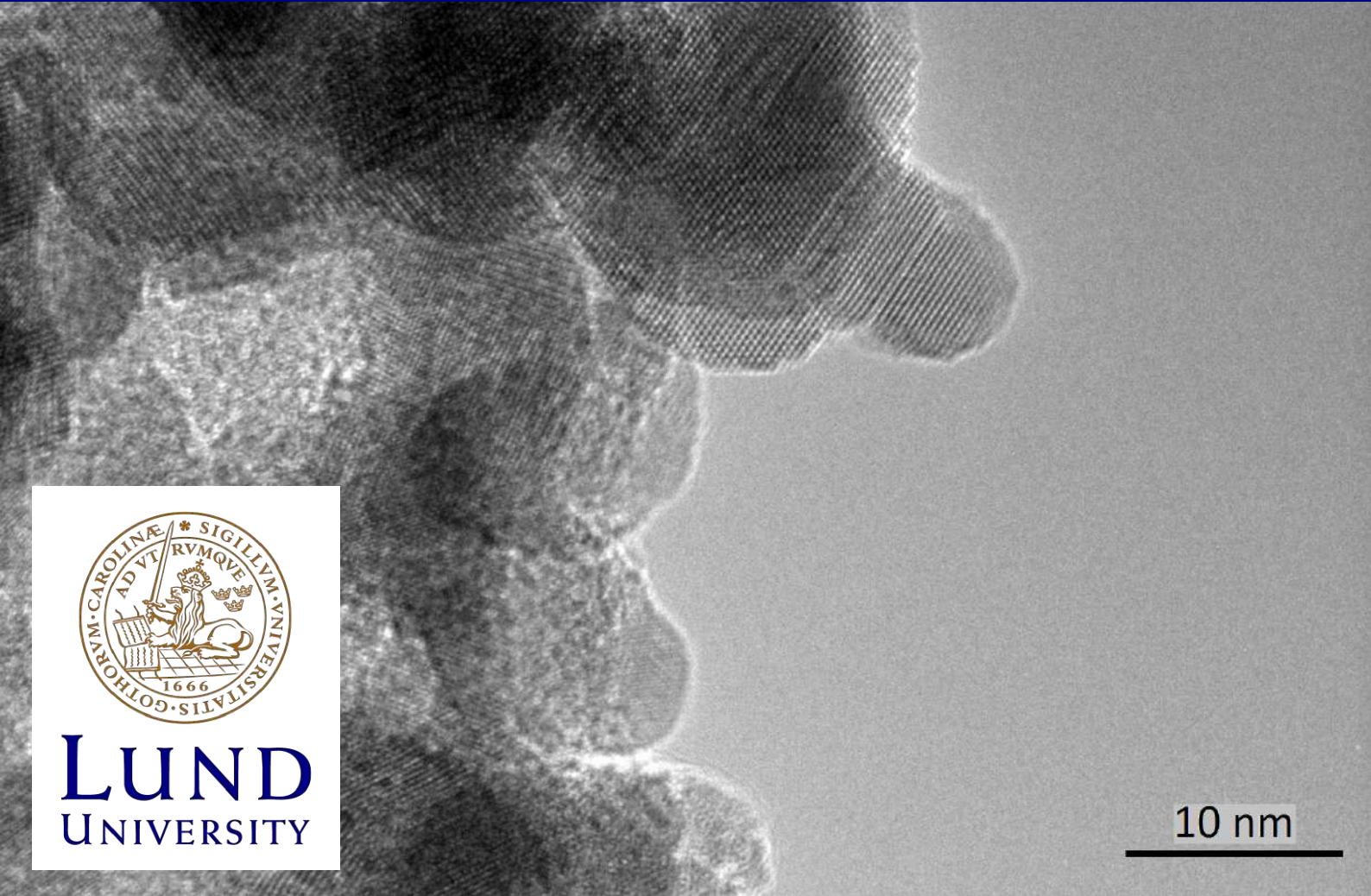
Lund University - Faculty of Natural Sciences

Physics Department

Lund University-MAX IV

10 nm

SIGILLVM · VNIVERSITATIS · CAROLINÆ · * · GOTHORVM · AD VTRVMQVE · 1666

LUND
UNIVERSITY

Lund University

Faculty of Natural Sciences

MASTER THESIS

Emmanouil Tzomos

X-ray Photoelectron Spectroscopy on Clusters: From Water Clusters to Metal & Metal-Oxide Nanoparticles

Lund University Physics Department

Supervisors: Sverker Werin, Maxim Tchaplyguine

Study program: MSc Physics

Study branch: Synchrotron Radiation Based Science

Lund 2020

December the 10th, 2020

I declare that I carried out this master thesis independently, and only with the cited sources, literature and other professional sources.

Abstract:

In the present work, two experimental setups aimed at the production of (1) water clusters and (2) metal-oxide nanoparticles were assembled and commissioned. The experiments on the cluster/nanoparticle beams were set up and performed at the Flex-PES beamline of the MAX-IV synchrotron facility. In these experiments, photoelectron spectroscopy technique was the tool, with Scienta R4000 electron spectrometer used for collecting spectra in water valence region and the low-kinetic energy region in the first part, and in silver valence and 3d region for the second part. The experiments on water clusters were motivated by the questions existing in the radiotherapy treatment of tumours by electrons produced as the result of body water ionization. Our experiments showed a monotonous growth of the secondary electron production with the kinetic energy of the primary photoelectrons. The experiments on silver-oxide nanoparticles were inspired by the role silver plays in catalytic oxidation processes. The results shed some light on the spectroscopic signatures of two possible oxidation states in silver about which a discussion has been running for decades.

Acknowledgments

Dedication

I wish to personally dedicate this effort to my wonderful family, who love me deeply, and support me no matter what.

Inspiration Quote

"Everyone of us is, in the cosmic perspective, precious. If a human disagrees with you, let him live. In a hundred billion galaxies, you will not find another." **Carl Sagan**

Notes on my participation

During this project, I participated fully in both experiments and analysis of.

Namely, I participated in the final commissioning of the beamline, the commissioning of the two cluster sources, the execution and monitoring of the two experiments, measurements, and their analysis under supervision.

In the collective activity described in chapter 4, I participated partly and was involved in taking measurements and some analysis and calculation.

Notes on the cover page

The picture depicted on the front cover is a Transmission Electron Microscopy (TEM) image of a bismuth oxide Bi_2O_3 produced by a metallic cluster source and was courtesy of Maxim Tchaplyguine.

Contents

Preface

This project spanned two academic semesters and involved both the commissioning of detectors and experiments at the FlexPes beamline in the synchrotron facility MAX IV in Lund. This beamline, whose functions will be presented in detail in the following chapters, focuses mainly on X-ray Photoelectron Spectroscopy or PES.

The work was planned around procedural activities, where the focus was put on all aspects of setting up and performing experiments on clusters using the light source of MAX IV and the tools of the FlexPES beamline. The first step was the commissioning of a cluster source at the beamline. It was followed by the main experiments which were designed to create environments similar to real macroscopic systems and probe the electronic properties of clusters. The benefit of which, whether it is water molecules in the body or metal particles that serve as catalysts in chemical reactions, is to have real tangible relations to practical applications. This was the main outcome of the work and the motivation behind it. The thesis is an effort to cover the knowledge/background and technical details relevant to the experiments. A lot of prerequisite knowledge has not been included for the sake of celerity but mentioned where needed and possible. The project itself also actively added to that knowledge and partly expanded further.

1. Clusters as an Intermediate State of Matter

Clusters are particles consisting of several identical atoms or molecules bound together. The number of entities can vary from a few to tens of thousands. In the limit of the larger size, clusters are often referred to as nanoparticles. The main objective of the present work was to study clusters of water molecules and then extend to metallic and metal-oxide clusters using X-ray PhotoElectron Spectroscopy (XPS). The specific aim was to probe their electronic properties, energy transitions, and details of composition - with the implications relevant for practical applications. Clusters can be produced in a laboratory via condensation of separate atoms or molecules at special conditions. Not all clusters, which scientists have studied, exist in nature.[1] However, there are quite some clusters that do exist around us, like soot particles or water clusters. One of the motivations to study water clusters comes from the fact that these clusters allow simulating situations related to macroscopic phenomena. For example, an important role of water clusters is in atmospheric processes and climate formation, so the knowledge of their properties and behaviour under ionizing irradiation can be very beneficial for environmental sciences. Argon clusters, as another example, are a good model system for studying properties typical for weakly bound solids of different kinds. Clusters or nanoparticles can be crucial for creating surfaces with desired properties. Clusters can facilitate and accelerate chemical processes acting as catalysts. Nanoparticles can be used in solar cell design, biosensor fabrication, cancer treatment, or electronics manufacturing. All these are practical applications that can be very beneficial to the general public. An extensive study of clusters has been going on for the last 50 years- in order to reveal their specific physical and chemical properties. Apart from the properties of the clusters themselves, while studying clusters one can get information about the corresponding macroscopic material which is otherwise difficult to obtain.[1]

1.1 Types of clusters and cluster geometries

Clusters can be sometimes thought of as an intermediate state of matter because the inherent properties of clusters may differ from those of separate atoms/molecules (out of which they are built) on the one side, and from the corresponding macroscopic phase (liquid or solid) on the other side. It is after a certain size that clusters begin to behave like a solid or liquid and start having the same properties as a piece of macroscopic material.[2] Cluster research seeks the answers to questions like how small a piece of material can be to still preserve the macroscopic properties, or how a material is structured at the nanoscale. For example, nowadays, when electronic devices have reached 10-20 nm dimensions, the question is how much smaller metallic wiring can be, or how small a diode or a transistor can be.

An example of clusters, which can be found in nature, is molecular water clusters, aggregates of water molecules that are held together by hydrogen bonds. A nanoscale water droplet relevant for environmental studies can be considered a cluster/nanoparticle. Big and small water clusters can be different in many senses. Water clusters are often argued to not be ice nanocrystals but liquid nanodroplets, and thus to have no ordered structure (Figure 1.1). The fundamentally smallest water cluster is the "water dimer" whose schematic presentation can be seen below in Fig.1.1. It has

been an important subject in the study of hydrogen bonding.[3]

In the case studied in the present work, the clusters contain a few thousands of molecules.[4]
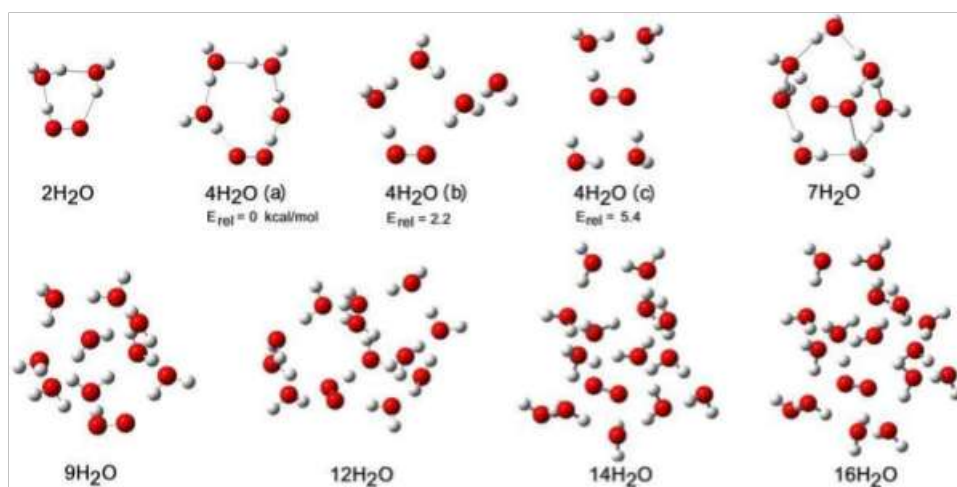
Figure 1.1: *Different geometries and structures of water clusters based on. [5]*

While water clusters may be amorphous, some clusters can have have a rigid geometry, like fullerenes (Figure 1.2a)- clusters of carbon atoms. Fullerene discovery gave the 1996 Nobel Prize in Chemistry. The most known fullerene consists of 60 carbon atoms and has an icosahedral geometry, much like the soccer ball(Figure 1.2b). It adopts such geometry in the self-assembling process out of carbon atomic vapour. The clusters with rigid geometry have different well-defined surfaces and other specific "sites", like vertices and edges, which can interact differently with the external world, so there can be behaviour specific to the orientation and geometry of the clusters.
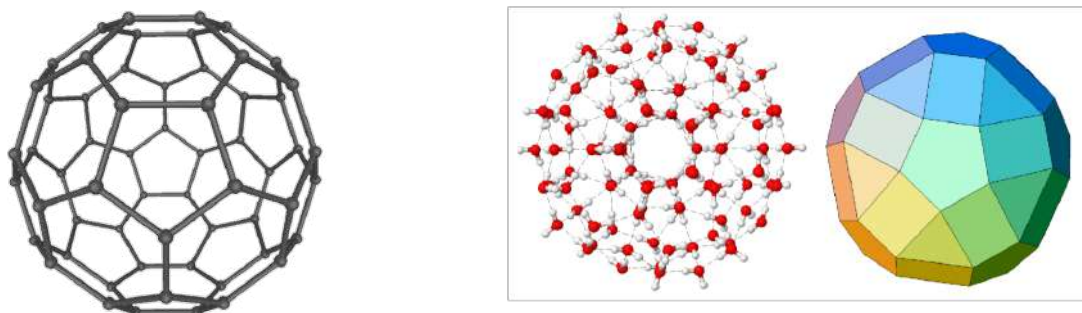
(a) The suggested structure of Fullerene or C_{60} Public Domain Image

(b) Hypothetical Water clusters following the icosahedral structure. Creative commons License.[6]

Figure 1.2: *Suggested geometries following the icosahedral structure.*

Clusters of other materials, like inert gases and metals, adopt the icosahedral geometry as well. Even water has been considered to have icosahedral geometry at certain conditions (Figure 1.2b). In the process of self-assembly, clusters of different sizes are formed at the same time. There is often a Gaussian-like (Log-normal) overall distribution of sizes. However, in such distribution there can be certain sizes which are more abundant than the others: the so-called "magic" geometrical numbers which are

characteristic to the icosahedral structure —13, 55, 147, 309, etc., atoms.[7] Scientists have explained this distribution of set geometries by the fact that these structures give the minimum of energy and volume compactness.[8] The larger the cluster, the lower its surface area is compared to the "bulk" - the internal volume of the clusters. This ratio is important because a lot of the cluster properties manifest themselves in the interaction of their surface with the external environment, so the corresponding cluster behaviour can be attributed to their surface atoms/molecules.[8]

In the water clusters of a few hundred molecules together, the surface fraction ratio is about 50%. By using Synchrotron Radiation from a source like MAX IV and PhotoElectron Spectroscopy (PES) technique, it is sometimes possible to differentiate the response that comes from the surface, from that which comes from the inner part or from what is called the "bulk" of the clusters.[5, 10]

The second type of clusters that is relevant is those kept together by ionic bonds. The most typical example would be the clusters of salt molecules, like NaCl, but also metal-oxide molecules that form ionic clusters when they "condense". In the current work, clusters containing silver-oxide and metallic silver were created and studied.

Figure 1.3: Structure of silver(I) oxide, Ag_2O.[9]

In figure 1.3 below, there is an example of a silver oxide's structure. The way that silver and silver oxides assimilate into clusters is complex and depends heavily on the presence of different oxide states and their orientation.

1.2 Water clusters & Their Special Significance

Water clusters have been extensively studied with different approaches over several decades, yet there is still room for productive research facilitated by the development of new experimental, theoretical, and computation techniques. In the case of water clusters, the formation process itself has been the topic of studies.[11, 12] In a separate water molecule, the oxygen atom has two outermost p- electrons bound with the hydrogen atoms, while the other two p-electrons are free to form additional bonds with the neighbouring molecules. This is known as hydrogen bonding, and this is what keeps clusters of water together. At appropriate conditions, a water cluster can be formed via self-assembly out of separate water molecules.

One of the modern motivations to study water clusters comes from the fact that these clusters allow simulating conditions related to radiation therapy, as they provide a water environment exposed to X-rays or electrons in ways not possible to achieve at laboratory conditions for any other form of water. In radiotherapy, it is believed that multiple secondary electrons produced as the result of primary ionization of water in biological tissue can play a role in destroying tumour cells.

In the radiation treatment of tumours, the primary electrons produced by an external source kick out secondary electrons from everything they meet on their way inside the biological tissue. Since 95% of the tissue is water, the larger part of the secondary electrons does come from water. The experiments on water clusters ionized by X-ray radiation can contribute to our understanding of how these secondary electrons are produced. In a hospital environment, the primary electrons would originate from an electron beam. In the current experiments, the primary electrons are produced due to

the water cluster ionization as the result of the X-ray irradiation. These are photoelectrons. The photoelectrons ejected by the valence levels of the clusters were used. The secondary electrons appeared in the low kinetic energy range from 0 to about 10 eV. These were the electrons produced by the electron-impact ionization in collisions of the primary valence electrons going out to the surface of the water clusters from their inner part.

To measure how effective this process is, the resulting secondary electrons produced by X-ray irradiation were detected and their signal was compared to that of the primary electrons.

1.2.1 Water Clusters' Size Estimate from Experimental Conditions

As mentioned above, water clusters can be formed via self-assembly/condensation if appropriate conditions are realized. To facilitate the aggregation of molecules into clusters, the process of adiabatic expansion has been used. In practice, the water vapour created by heating in a dedicated container (oven) is let to expand into vacuum through a tiny orifice- a nozzle. The strong cooling of the vapour due to the abrupt pressure decrease facilitates the condensation, and such an expansion creates a beam of water clusters of a certain size distribution. This distribution depends not only on the inherent properties of the expanding gas/vapour but also on the configuration of the experimental setup used for producing the cluster beam. The vapour pressure in the container, the nozzle temperature, dimension, and shape - all play a role in determining the cluster size produced in the experiment.

The cluster mean size formed by such an expansion can be theoretically estimated with some approximations made and some theoretical background considered. The method has been demonstrated for water clusters in the work by Bobbert et al. [4] where the necessary equations for determining mean cluster size based on the expansion parameters were derived. The approach uses the so-called scaling parameter Γ formalism [4] which depends on the concentration of the molecules in the vapour n_0, nozzle temperature T_0, and the nozzle orifice diameter d. The mean cluster size in the log-normal distribution was calculated for a set of experimental parameters.(The calculation process description is attached in the Appendix)

As will be discussed in more detail further down, for several bars of water vapour pressure it occurs to be possible to cover the cluster size range from a few hundred to several thousand molecules per cluster. The cluster size can be varied by changing the water container temperature and thus the water vapour pressure.

1.3 Metal Clusters and Conducting Sphere Approximation

An example of a cluster type produced artificially is metal clusters. There are numerous production techniques with thermal evaporation or cold sputtering using a magnetron being probably among the most popular.[13–15] The metal clusters evoked a lot of fundamental scientific interest.

The information on the electronic structure is important because the latter defines the size-dependent physical and chemical properties of the clusters/ nanoparticles. Knowing and understanding these properties is critical when it comes to, for example, making new nanostructured materials, nanoscale electronics, or making catalytic chemical reactions more efficient.

This practical side of clusters/nanoparticles provides a strong motivation behind the study of metallic clusters.[16] Silver and Platinum metal nanoparticles are excellent catalysts in processes that have a large market value. Production of detergents is one of them. In the specific case of silver, ethylene epoxidation using nanoparticles of silver is a significant industrial activity producing a precursor for detergents. The catalytic role of silver oxides in ethylene epoxidation was the motivation for the studies of silver-oxide clusters/nanoparticles, and the experiment on silver clusters was designed to address certain questions existing in that field.

1.3.1 Metal Clusters' Size Determination

One of the main questions, which appear in the cluster creation process, is their size determination. In the experiments on clusters, it is critical to know the average size of clusters that one is probing. As discussed previously, it is after a specific size that clusters get their macroscopic properties. An established method to estimate the dimensions of clusters is based on treating them as conductive spheres. This was used [17] to form a relation between their size (radius) and their ionization energy. More exactly, the relation connects the cluster radius with the difference between the cluster ionization energy and that of the corresponding macroscopic elemental metal. This result can be conveniently used in photoelectron spectroscopy experiments when the lowest valence ionization energy, equal to the work function of clusters, is established.

The relation is shown below for neutral clusters:

$$E_{cluster} = E_{solid} + \frac{1}{2}\frac{e^2}{R} \tag{1.1}$$

It is important to note that this relation has been validated both theoretically and experimentally.[18] Also worth mentioning is that there are other approaches to measuring cluster size, namely using time of flight mass spectroscopy or TEM techniques. All have their own advantages and limitations.[19]

2. Cluster Production

To create clusters in the experiments in question, one needs first to create primary atomic/ molecular vapour and then the conditions at which this vapour condenses. The vapour can be cooled by collision with a cold gas, or through expansion into vacuum, forcing atoms or molecules to create clusters of a set size, composition, and geometry dependent on the conditions. For different parent materials, different experimental setups, often referred to as cluster sources, are needed. As will be seen in the next section, to create water clusters, adiabatic expansion of water vapour into vacuum was used (the first experiment), and for making metal and metal-oxide clusters "cold" evaporation by magnetron sputtering of a metal in the atmosphere of a cryogenically cold gas was used (the second experiment). By admixing oxygen into the used for sputtering argon gas in the metal-cluster source, metal-oxide clusters can be created. This was done in the case of silver. To achieve all this, dedicated experimental setups must be designed, and were designed by various research groups in the past.[20] For the sake of briefness, only certain details of the equipment and methods relevant to the present work will be described.

2.1   Adiabatic Expansion Cluster Source for Water-Cluster Production

The adiabatic-expansion source for creating water clusters has a relatively simple principle of operation. The central part of it is a stainless steel container filled with water in which heating continuously creates water vapour and consequently, pressure builds up.
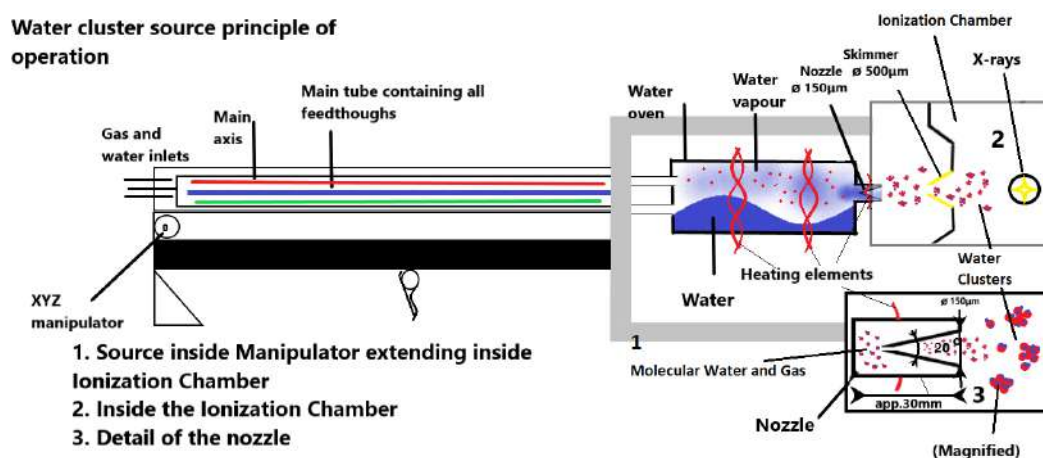
Figure 2.1: *A sketch illustrating the operating water cluster source. The conical nozzle is shown separately – enlarged in an insert. Also, the Ionization Chamber is shown to which the cluster source is attached.*

The container is placed inside a dedicated vacuum chamber (Figure 2.1) and is mounted on a rod of an XYZ-manipulator, which is in its turn attached to the port of the vacuum chamber. The only escape for the vapour from the container is a carefully positioned and constructed nozzle which lets out a jet of water molecules and – at certain conditions- of water clusters. The nozzle – a tiny channel of a special diverging -cone geometry- is the key element for the cluster production. The vapour amount being continuously ejected is incomparably small to that of the water container, and the vapour concentration is "instantaneously" restored by evaporating more water. The

vacuum chamber in which the water container is placed is continuously evacuated. The water vapour expands abruptly -adiabatically – into vacuum which causes vapour to cool abruptly. Both the vapour pressure and the nozzle aperture and conical shape define the parameters of expansion. At certain conditions (vapour pressure, nozzle temperature) the abrupt cooling of the vapour leads to vapour condensation and thus cluster formation.

In the first experimental setup, the water container -referred here also as a water oven- as well as the nozzle could be separately heated resistively, each using a special thermal element. It is important to monitor both the container/oven and the nozzle temperature separately using two thermocouples. Due to the adiabatic expansion, the nozzle is also cooled and the water vapour in it would freeze if it were not heated specifically. Then the aperture of the nozzle, which is about 150 micrometers in diameter would be blocked. It is to avoid this blocking that one has to heat and monitor the nozzle. It is important to note that the 150-micron nozzle itself works as a small leak into vacuum - by design. This leak makes the time to evacuate the oven (after the start-up of air pressure) rather long. When the pumping starts, first, at higher air pressures, the flow is laminar like of a liquid, but when the larger part of the air is pumped away then the molecular-flow regime becomes the case, so one has to wait for the air molecules to randomly move and leave through the nozzle. If the oven is filled with water "in-the-air" -before the pumping starts, then 20 mbar of the water-vapour partial pressure existing at room temperature will be creating a weak vapour jet, first of the mixture with the air, and then of pure water vapour.

For providing the heating-wire and thermocouple-wire connections from the air-side to the vacuum-side special electrical "feedthroughs" were used, mounted at the back flange of the XYZ-manipulator. Inside the vacuum chamber, the wires had to stretch all 40 cm of the manipulator towards the water oven. For filling the oven with water from the air-side without breaking vacuum one has to also have two inlet tubes that were installed inside the manipulator and were connected to the oven.
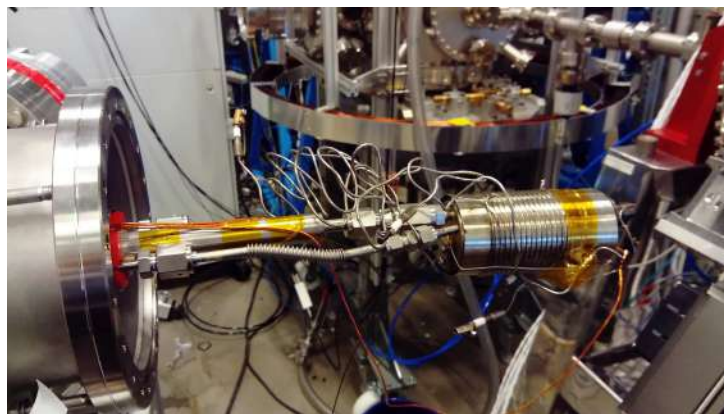
Figure 2.2: The water oven extended to the maximum position, the heating elements visible.

The pumping system of the cluster source consisted of two turbo pumps attached to the dedicated vacuum chamber and a fore-vacuum pump that created a necessary low preliminary vacuum at the output of the turbo pumps. The turbo pumps created high vacuum in the cluster source. The vacuum was measured with the so-called cold cathode vacuum gauge. In the experiments at the beamline, the cluster source was attached to the beamline endstation, and the water oven could be moved close to the ionization point, where the cluster jet was crossed by the x- ray radiation, the clusters

were ionized, and the ejected electrons were collected and analyzed by the electron spectrometer. To provide all these possibilities, a lot of "peripheral" equipment had to be used. (The descriptions can be found in the Annex)

2.2 Magnetron-sputtering based Source for Metal-Cluster Production

Producing metal clusters is a process that can be accomplished via a number of ways. In the current work, a specific setup based on magnetron sputtering was used. A magnetron cold-plasma sputtering source for metallic particles is able to provide a steady and intense continuous source of clusters to be studied by PES. The parent metal vapour necessary for particle aggregation is produced by sputtering of a metallic plate. The main advantage of such a source is the absence of a need to heat the metal for its vaporization.

The basic principle of magnetron sputtering is that an electric discharge is ignited between the negatively - biased cathode (to which a metal plate, in the present case – a disc, to be vaporized is attached) and an anode which is a hollow metal cylinder positioned concentrically with the metal disc (Figure 2.3) and held at zero potential. The metal disc is often referred to as a target. Argon gas is used because even when ionized it will not react with the metal vapour and produce any chemical compounds. The ionized argon atoms bombard the target and kick out metal atoms from it. The magnetron discharge plasma is contained close to the target by a strong magnetic field of two specially shaped permanent magnets placed behind the plate. In this case, the magnetron sputtering source was a commercial one by Meivac Inc.[21], model MAK.

This sputtering source was modified to adapt it to the task of metal cluster production. Magnetron sputtering was traditionally in the surface deposition technique, as described by, for example, ''Vacuum Deposition of Thin Films.''[15] Incorporated into an appropriate setup, magnetron sputtering can be a tool for creating a beam of atoms or clusters. The sputtering of the target creates a "cloud" of metal atoms, in the present case silver atoms. When oxygen is admixed into argon in different amounts, it dissociates into atomic oxygen in plasma, and metal oxide molecules can be created. This is called reactive sputtering.
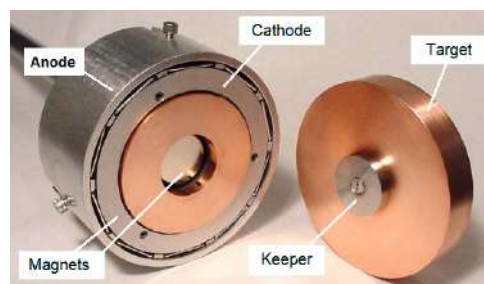
Figure 2.3: *The MAK magnetron sputtering source when not assembled, with a target and other parts visible*

The more power one applies in the discharge, the quicker material is lost from the target. A typical target can have a lifetime of several hours depending on the sputtering rate of the material and the sputtering power. The magnetron target was a disc 6 mm thick and 50 mm in diameter, similar to that in Figure 2.3.

To operate a magnetron a number of conditions should be provided: that is its water cooling, a constant flow of the sputtering gas, and a certain level of vacuum around it achieved by continuous pumping. The technical aspects along with a lot of information on its operation can be found in the brochure of Meivac available at its website.[21] In Figure 2.3 one can see the commercially available (before the in-house modification) MAK sputtering source.

The design of the magnetron-based cluster source can be seen below in Figure 2.4 where the individual parts are shown. Apart from the magnetron, the cluster source

consists of a dedicated vacuum chamber, an XYZ manipulator, and a pumping system. The magnetron is placed inside a double-wall liquid-nitrogen-cooled cryostat 2.4b, which, in its turn is mounted on the manipulator rod inside the vacuum chamber.

(a)   *(b)*
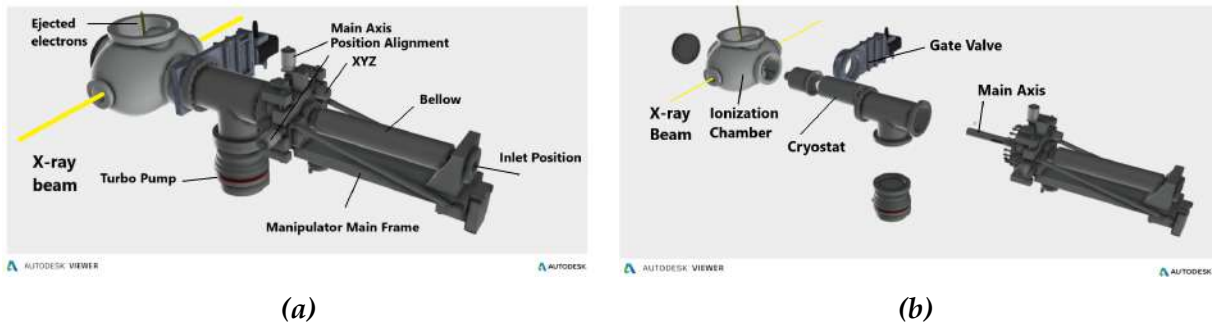
Figure 2.4: *On the left 2.4a the Metal cluster source is shown as it appears when fully assembled and attached to the ionization chamber of the beamline (Electron spectrometer not shown). A gate valve that separates the cluster source and the ionization chamber is also seen. On the right - the same setup with all the individual parts disassembled and shown separated*

As mentioned above, the magnetron itself and thus the whole cluster source requires inlets for the sputtering argon gas, as well as for water cooling. In the current setup, a separate cooling station with a water pump was used for cooling. Additionally, the cluster source requires inlets for helium gas, which is added to efficiently cool the metal vapour entrapped in the cryostat. There are also input and output tubes for the liquid nitrogen that is continuously pushed through the cryostat to cool the latter down to a cryogenic temperature. All these inlets along with the vacuum pumping ports and the electrical and thermocouple connection wiring, have to go through the full length of the manipulator to the magnetron and cryostat positioned inside the vacuum chamber (Figure 2.4). This creates a challenge when it comes to synergizing everything.
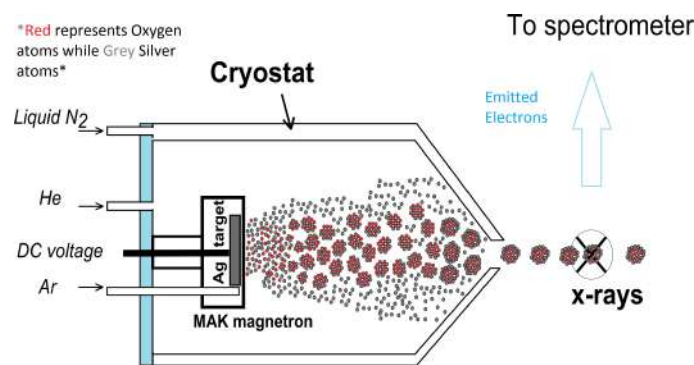
Figure 2.5: *The cryostat enveloping the magnetron, creating the source environment. Visible are the inlets for the gases described above and an example of the particles created. Grey balls represent silver atoms while red -oxygen.*

In Figure 2.5 a sketch of the source cross-section is presented that shows the details of its construction, environment, and how the cluster beam is created and further on intersected by the X-ray radiation. The consequent ejection of the electrons from the clusters towards the spectrometer is also illustrated.

All the specifications have been described in the paper [13] in detail, where also valence spectra of silver are presented. At MAX-IV, the old cluster source was significantly refurbished.

3. Experimental Methods and Relevant Physical Processes

3.1 Photoelectron Spectroscopy – a Method to Study Ionization under X-ray Irradiation

One of the specific types in the field of Spectroscopy is Photoelectron Spectroscopy or PES. In general words, it is an approach aimed at detecting electrons that leave the sample due to the photoelectric effect. It refers to any measurement that seeks to define the binding energy of electrons emitted by any type of matter -gas, liquid, solid, or even plasma, using Einstein's photoelectric effect equation $hV = E_{Binding} + E_{Kinetic}$. Different sources of radiation such as Lasers, UV lamps, or X-ray sources are used. Historically, some spectroscopic techniques were aimed at probing the valence - or outer levels, which need lower photon energy from the Vacuum Ultra Violet (VUV) for ionization. The valence electrons carry information on the chemical bonding between the atoms in the substance. This technique is often referred to as Ultraviolet Photoelectron Spectroscopy (UPS). Another method that utilizes higher photon energies of the X-rays, which can probe the core levels and is often referred to as XPS -X-ray photoelectron spectroscopy.

The core levels of atoms are element-specific and thus can serve as "markers" of what element is present in a sample. XPS was developed to a large degree in Sweden, and for the merits in its development, a Lund native and long time professor in Uppsala Kai Siegbahn received the 1981 Nobel in Physics. The XPS was initially developed as a chemical analysis technique – Electron Spectroscopy for Chemical Analysis (ESCA) [22], and the radiation of the so-called rotating anodes was implemented then. The introduction of more powerful sources of X-rays, such as synchrotrons, that possess tunability, greater flux, has opened new possibilities for XPS. Higher intensity and tunability al- lowed to use higher resolution and resolve states not possible to resolve with the rotating anode radiation, thus providing more insight into the electronic structure and other properties. The synchrotron-based PES allowed addressing "exotic" samples of dilute concentrations- such as cluster beams.[1]

For implementing modern PES-XPS researchers use – rather often -an electron energy analyzer, one type of which will be presented in Chapter 4 in detail. The properties of Synchrotron Radiation will be discussed in the next section, while related to its production facilities and devices -like storage rings and undulators, will be described in Chapter 4 using MAX IV as an example.[23]

3.2 Synchrotron Radiation and PES

Synchrotron Radiation is the electromagnetic radiation appearing when charged particles, most often electrons, move along a bent orbit. When these particles move at relativistic velocities the radiation is emitted into a forward-directed narrow cone. In general, the Synchrotron Radiation, (SR) produced in a dedicated circular storage ring contains photons of a wide electromagnetic spectrum, from infrared to hard X-rays. To produce intense radiation, an electron beam goes through an undulator – a device placed in a straight section of a storage ring that forces the electron beam to oscillate in a specially designed magnetic field. Depending on the period of the

oscillations different spectral ranges of thus produced X-ray radiation can be enhanced. As will be seen in Chapter 4, different users require different ranges of SR, and this is provided by the so-called beamlines, which guide the desired part of the radiation spectrum to the sample. A typical synchrotron facility has many such beamlines with sometimes several experimental stations each. In Chapter 4, it will be also shown how the same beamline can accommodate several techniques, as is the case with the FlexPES beamline where different types of PES can be realized. A modern Synchrotron facility can accommodate experiments that concern many branches of science and SR is widely used in biology, chemistry, and physics.

The main advantages that SR gave to XPS/PES were the tunability in a wide range, a definite polarization of the radiation, and its high intensity. Below in Figure 3.1, the schematic illustration of an XPS measurement is presented, where the electronic structure of a copper atom is also shown, as well as its XPS spectrum with different levels detected.
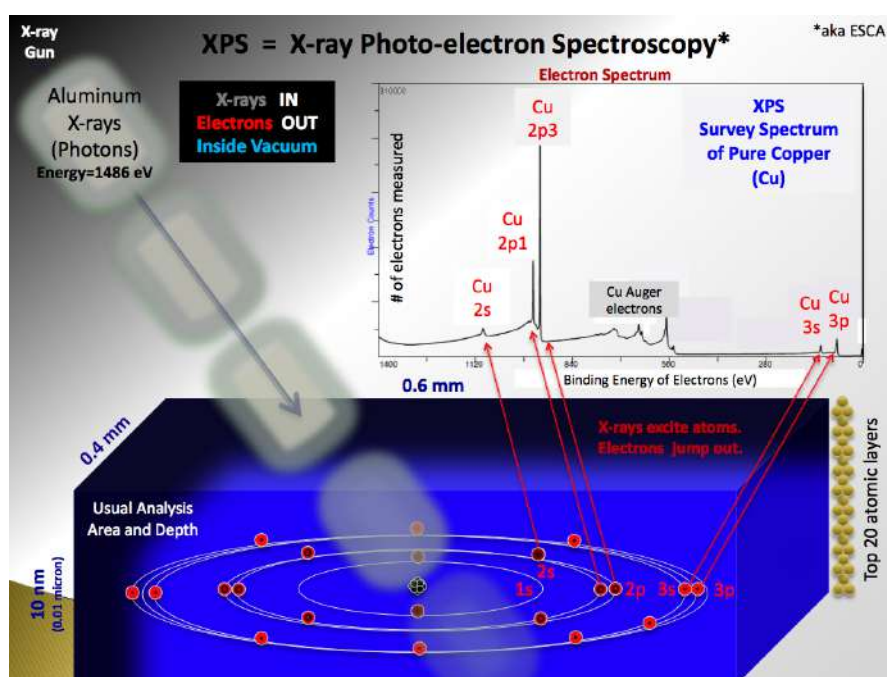
Figure 3.1: *The principle of XPS depicted graphically in which the different energy levels of a Cu atom and a typical electron spectrum after ionization by X-rays are visualised. Public Domain Image*

An early description of how to implement XPS is given in the book by Jolm F. Moulder et al.[16], entitled "Handbook of X-ray Photoelectron Spectroscopy". Although the book describes the XPS use for mainly probing surfaces of solids, it is a useful initial guide to understand how to perform XPS and how to interpret the resulting spectra. As said above, nowadays XPS can probe any type of matter although the penetration depth of the photons which XPS uses (typically below 2000 eV) is limited to roughly a micron. Thus researchers sometimes need to combine their XPS studies with other techniques like Diffraction imaging or Electron Microscopy that have their own advantages and limitations. The main outcome of an XPS measurement is a spectrum in which one needs to identify individual features based on the binding energies detected, assign these features to the different states of constituent elements. The assignments are made involving, among others, the consideration of the ionization

probability for each electronic state. This probability depends on the type of electrons (s,p, d, f) in the state, and the photon energy implemented.

3.3 Relevant Energy Levels, Transitions and Other Factors Defining a Photoelectron Spectrum

As discussed, the main result of an energy analyzer measurement is a kinetic energy spectrum that contains "lines" or "peaks" at the energies at which the electrons emitted from a specific state were detected. The peak in- tensity will tell us about the concentration of this or the other element in a material that got ionized. From the detected kinetic energies, using the relation $hV = E_{Binding} + E_{Kinetic}$, the binding energy of the corresponding state can be calculated. Knowing the binding energies of specific states enables us to distinguish what chemical elements we see in the energy spectra of the sample. This element or the other, a specific molecule, or a cluster will have a unique signature that serves as a "marker" for their presence in the ionization "point". Specific chemical elements have a known binding energy. For example, atomic Argon has a binding energy of 15,94 eV and 15,76 eV for its $3p_{1/2}$ and $3p_{3/2}$ states respectively. One needs a relatively good experimental spectral resolution to resolve the two states in a spectrum, as they only have a 0,2eV separation, but even if these peaks are not resolved, they can help us to calibrate the binding energy scale in the measurements. Here I give a brief example: when a beam of metal clusters produced by the second setup is ionized by X-rays, the valence region spectra contain not only the Fermi level/Work-function of the clusters (the onset of the valence band), but also the mentioned above 3p lines of argon gas, which is present in the cluster beam. Due to the latter fact it is possible to accurately calibrate the binding energy scale and determine the Work-function. One should mention here that the conclusions from the photo-electron spectra can be easily drawn because in a typical photoelectron spectroscopy experiment on a cluster beam at a synchrotron beamline only one photon is absorbed per cluster. If one used a Free Electron Laser (FEL) there would be significantly more photons in the ionization point, so that absorption of more than one photon per cluster has been observed.[24]

In compound substances, the valence-level spectra are, as a rule, not as simple as for argon gas. However, the core-level spectra are usually relatively simple even in compounds, since the core levels do not take part in the chemical bonding between different (or the same) elements in a substance, and the spectra occur atomic-like. In other words, a core-level spectrum is often just separate relatively narrow "lines". A core-ionized state usually has a very short life-time: the electron vacancy created in a core level is very soon filled with a valence electron, and another valence electron is ejected (The latter is known as an Auger electron). The life-time of the vacancy (or of the core-ionized state) is reflected in the inherent natural width of the corresponding line in a spectrum, which width is described by a Lorentzian spectral profile. The larger the width of a Lorentzian profile of an observed peak is, the shorter is the life time of the core-ionized state. Apart from the Lorentzian width, a spectral line profile is influenced by the spectral width of the radiation which one gets from the beamline monochromator. Moreover, the electron spectrometer contribution broadens the spectrum -due to its final energy resolution discussed below. The Lorentzian profile experiences what is called "instrumental broadening", and the signal that is observed is a convolution of the inherent Lorentzian profile and the Gaussian profile due to the

finite radiation spectral width and the electron spectrometer resolution. The resulting profile is known as Voight profile. Therefore, in the analysis part, we must take this into account and define the parameters which influence the full width of the spectral "line" – the signal. For the metallic samples, there is a specific core-level profile known as Doniac-Sunjic profile, and in the experiment, it is convoluted with a Gaussian profile. One has to distinguish these profiles and treat the spectra accordingly to make the fitting process physically meaningful.

The total instrumental broadening of the signal can be estimated as:

$$\Delta E_{total} = \sqrt{\Delta E_{spec}^2 + \Delta E_{mono}^2}$$

Using this relation and a computer software to make fittings, one can quantitatively characterise these spectra. The broadening ΔE_{spec} due to the spectrometer characteristics can be taken from the tabulated values in the spectrometer manual. The monochromator broadening ΔE_{mono} is taken from the beamline characteristics.

In general, we construct possible ionized states using the orbital quantum number "l" and the spin quantum number "s". The latter is usually $\pm 1/2$ for the initially fully filled core states which lose one electron in the process of ionisation. One can calculate the total quantum momentum j by adding the orbital and spin momentum. For example: the s state has an l=0 and the total spin of the remaining on the orbit electrons will be ½, so there is only one ionized electronic state, which will give us a 1s state for oxygen(meaning that there is only a ½ total momentum). The 2p state (in , for example, argon) has the orbital momentum l=1, and a spin of the remaining electrons s=1/2. This spin can be ''positive'' or ''negative'' relative to l, so this will give us a 2p state with the total momentum J either 3/2 or 1/2. The d state has the total momenta 3/2 or 5/2 for the ionic states and so it goes.

3.3.1 The Ionization Process in Water Molecules and the Relevant Energy Transitions

For water molecules and clusters the valence-level ionization process, which is the transition between the neutral and the ionized electronic states, is considerably more complicated than, for example, for argon gas, due to the presence of the chemical bonding between the constituent atoms. In a water molecule, both the initial/ground neutral and the ionised final electronic states have vibrational levels. A molecule in the ground state is usually at the lowest vibrational level. There are valence ionic states, at least three to mention- X, A, and B states, which are populated as the result of valence-electron removal. Each of these states has several vibrational levels, which become populated in the ionization process and clearly manifest themselves in a photo- electron spectrum. Not all vibrational levels are populated/excited, but only those that correspond to the so-called vertical transition from the ground electronic state.

The 1s-level core ionization of water molecules produces a relatively narrow peak where vibrations are not resolved, after which ionization the emission of Auger electrons takes place. I will not describe these processes in detail as they do not concern these experiments. For the purpose of this work, only the valence- ionised water molecules and clusters were studied.

As a rule, the separate molecules have a higher core-level ionization energy than

for the clusters consisting of these molecules. In the case of water and its 1s core state, it is because the water molecules have an inherent dipole moment. When an oxygen atom of one molecule in a cluster is ionized, a positive charge appears on this atom, and the other molecules of the cluster ''turn'' to face it with their negative parts. Besides, a distortion or better, a stretching of the electron cloud of the neighbouring molecules that constitute the cluster appears. Both phenomena together produce what is called a Screening Effect. The electrostatic field of the "turned" water molecules reduces the electrostatic potential at the position of the ion, and the total energy of the final ionized state decreases. The outgoing photo electron "senses" it, so its binding energy, calculated as the difference between the total final-state energy and the total initial-state energy, also decreases.

The screening effect is strongly dependent on whether the cluster is conductive or dielectric. In the first experiments, water clusters were studied, and they are non - conducting. In the second experiments, metallic clusters and oxide clusters were studied. In the silver cluster environment, the Screening effect is more complex with the presence of different oxides and metallic silver.

3.3.2 Difficulties in Producing and Analyzing Silver Oxides

As it was described in the first chapter of this thesis, the use of silver particles for the epoxidation (specific oxidation) of ethylene motivates the study of silver- oxidation states realized in the clusters, and the ways to determine these states by PES. The latter task has been the main concern of the present experiments. The various oxidation states and different mutual orientations of silver and oxygen lead to a difference in the catalytic environment, and this is what decides the effectiveness of ethylene epoxidation. One of the basic ideas here is that the more dissociated oxygen (in atomic form) is available for the process the better. Silver leads to dissociation of molecular oxygen, and such oxygen binds to silver. This is how silver oxide is produced. The atomic oxygen availability depends on the cluster size, surface fraction, the presence of different oxidation states in clusters, etc. The role of all these parameters does not follow any simple pattern, and new improvements are found from time to time.[25]

It has been challenging to discern the oxidation states of silver due to the limitations in the sample preparation, the inapplicability of, for example, diffraction techniques to the samples produced at laboratory conditions (see next section) and other inherent difficulties of the used techniques, also PES (see further down).

Epoxidation of ethylene happens at high pressures and temperatures, so it is difficult to use traditional methods of surface science, such as PES, to study what happens when silver comes in contact with oxygen. Laboratory studies have been hindered by the fact that it is difficult to oxidize silver since it is a noble metal. Moreover, two silver oxides/oxidation states are possible, and there has been a discussion on what kind of oxide is produced in what conditions. Despite all the difficulties and uncertainties, there has been extensive data gathered for the main silver oxides, namely that of Ag_2O and AgO, from decades of PES experiments. To distinguish between the two main oxides of silver occurs to be a difficult task and PES is, in general, is one of the few tools which could do that.

In parallel with the studies, there has been a significant effort to establish a reliable procedure of producing this or the other silver oxide in vacuum, at controlled condi-

tions suitable for PES. Standard chemistry methods did not satisfy the PES demands of purity and uniformity. One chemical method results in precipitation of a monovalent Ag_2O oxide in powder: it uses the aqueous solutions of silver nitrate and an alkali hydroxide.[26] In order to study it by PES, one has to dry the powder by heating and then press it into a pellet. Exposing the sample to air and heating contaminates the sample. To produce AgO by wet-chemistry is more complicated. Moreover, it occurs to be a substance with two different oxidation states (I) and (III), or mono- and trivalent. It has the formula Ag_4O_4, and silver atoms are present in two different orientations in it, namely that of Ag_2O and Ag_2O_3. [3, 27]

In surface science a typical way to produce metal oxides is to expose a metallic sample to oxygen, possibly at elevated temperature, then pump oxygen away, and study, by PES, what happened to the metal. However, as mentioned above, silver is difficult to oxidize this way. One approach that worked was plasma treatment of silver in a rich oxygen atmosphere. Then, a very thin layer (sub-micrometer) of an oxide covering the metal would be formed. However, the case is that researchers had to identify what oxide was formed at this or that condition (oxygen pressure, plasma intensity, treatment duration, etc.). And since the spectroscopic characteristics of silver oxides would not be established reliably in such experiments - due to the samples with the uncertain composition - a ''catch 22'' situation has been typical for this field for decades. In a paper by Bielman et al. [28] where ''oxidation of Ag in an electron cyclotron resonance O_2 plasma'' was used and PES was utilized to probe the states and contributions of different silver oxides, some of these challenges were presented and discussed. Also, in the paper by Kibis et al [29] plasma oxidation of a thin silver foil was used. In the work by Tchaplyguine et al, [30] the silver-oxide nanoparticles were created using magnetron reactive sputtering of silver in the argon-oxygen mixture - by the setup predecessor to the one used for this Master work.

As for the spectroscopic signature of silver oxides, the most common ''witness'' has been a photoelectron spectrum of the silver 3d core level (binding energy 370 eV). In contrast to most of the known metal oxides, the binding energy of Ag 3d level in the Ag_2O oxide was detected to be lower than that in the metallic silver, lower by just 0.5eV. [31–33] Such a difference is hardly distinguishable at the background of the experimental line width of often about 1 eV. Besides, such a small difference could be questioned in view of the difficulties with binding-energy calibration for a non-conducting sample, which an oxide is. As for the AgO oxide, there the Ag 4d valence band should be opened due to the Ag 4d electrons involved in bonding with oxygen. As a consequence, not only the difference with the metallic Ag 3d can be expected larger (as it usually is for a higher oxidation state oxide), but also the so-called satellites should be seen in the Ag 3d spectra. –Such satellite lines appear due to the different final states in the ionization process. [31, 34] These satellites have not been seen until recently [28], while the claims of observing AgO in the spectra were made not once in the past, see [33, 35–37] and references therein. At the same time, with satellites or not, the Ag 3d spectral response in AgO oxide was always supposed to have lower binding energy than the metallic silver Ag 3d. In terms of the PES field, the difference between the metal and the oxide spectral response is referred to as an oxide shift. Thus the lower binding energy for the oxide is a negative shift. The conclusion of a negative shift being the case for silver oxides might have been generated by a systematic error in the binding energy calibration.[38] In all cases found in literature there has been no simultaneous presence of Ag 3d metallic and oxide signals in one and the same

spectrum. Thus, the calibration should have been done using external references, and that might be the source of error, especially if one talks about 0.5 eV shifts as in the Ag_2O case. Kibis et al.[29], as well as Tchaplyguine et al [30], attracted valence PES in an attempt to assign the oxidation states of silver.

In Chapter 5 our own experiments aimed at spectroscopic identification of silver oxides will be presented.

4. MAX-IV Synchrotron Facility and FlexPES Beamline

Figure 4.1: *MAX IV lab in Lund, Sweden. "We can probe the invisible!"*

Synchrotron Radiation has a relatively recent history. First "accidentally" discovered at a General Electrics lab by a famous team of researchers in 1946 - Frank Elder, Anatole Gurewitsch, Robert Langmuir and Herb Pollock [39] - that also gave it its name. Nowadays, researchers produce Synchrotron Radiation using electron storage rings with the help of special magnetic arrays called undulators that produce radiation in a desired spectral range, such as Vacuum Ultraviolet (from 10 up to 50 eV photon energy), Soft X-rays (from 50 to 2000 eV), and hard X- rays (above a few thousand eV).[40]

All synchrotron facilities have a storage ring where an electron beam moves along a closed trajectory. In reality, a storage ring is not circular but a "polygon" in which the straight sections have bending and focusing magnets at their junctions. The undulators are positioned in the straight sections of the storage ring. With undulators, one creates a constant "wiggling" of the electrons wherein every step radiation is emitted, and the interference of those individual emissions creates a highly collimated and intense beam of X-rays. Due to the emission of photons by the electrons circulating in the storage rings, energy is lost in each bend and continuously more energy has to be pumped into the electron beam. For that in Synchrotrons, one uses Radio Frequency cavities.

MAX IV is a facility where a unique technology was developed and applied, the so-called 7-bend achromat. It made MAX-IV the most brilliant source in the world. In Lund, there has been a long tradition in the field of accelerators, synchrotron radiation and spectroscopic studies using synchrotron radiation.

4.1 MAX IV lab and its Capabilities

MAX IV lab was constructed with a consideration of maximizing user capabilities, providing them with maximum versatility. MAX IV incorporates two storage rings with different energies of the circulating electrons that produce Soft and Hard X-rays, and more than 10 "beamlines" that are stations where different experiments can be performed. The two rings R1 and R3 are schematically presented below in Figure 4.2 and have energies of 1.5 and 3 GeV respectively. The storage rings are injected with relativistic electrons by the Linac (Linear Accelerator).
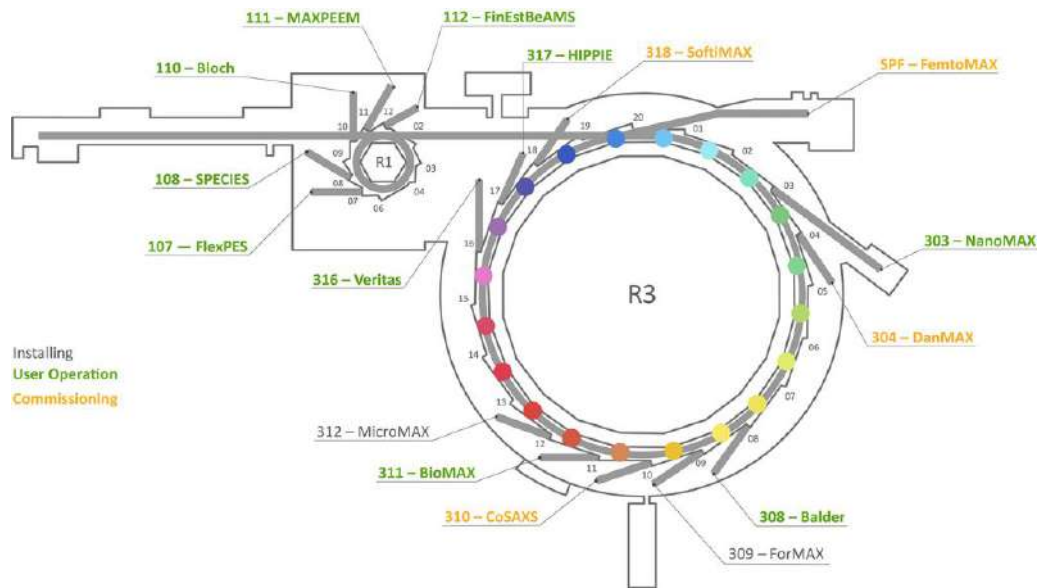
Figure 4.2: *A schematic representation of the MAX IV lab seen from the top with the two rings as well as the individual beamlines (both current and future ones)*

Each beamline has its own dedicated function and uses the relevant techniques for a certain field of Science. Among these fields are Life sciences, Medicine, Geology, Nanoelectronics, Nanoscience, General and Accelerator Physics, etc.

Each undulator is unique as well as the optical scheme of each beamline.

4.2 The FlexPES beamline

The FlexPes beamline, seen in the diagram in Figure 4.3, is a beamline located at the 1.5 GeV ring. The beamline operational photon energy range is from 40 eV to 1500 eV. The undulator has 48 periodically placed magnets with a minimum adjustable gap of 16 mm and an effective magnetic field power of 0.8T.[41] The undulator - like most of the other parts - can be computer-controlled, and its gap is automatically adjusted to match the photon energy set by the monochromator. The undulator is programmed to provide a gap size that gives the maximum intensity for the chosen photon energy. The photon energy, which reaches the sample, is to a great extent defined by the angle of the grating of the monochromator. By changing the opening of the monochromator's exit slit the spectral width of the radiation can be chosen.

There are five kinds of PES techniques that the FlexPES beamline can provide for the users: Core-level photoelectron spectroscopy and Auger electron spectroscopy, Resonant Photoemission/Resonant Auger Spectroscopy (RPES/RAES), Angle-Resolved Photoelectron Spectroscopy (ARPES), and X-ray Photoelectron Diffraction (XPD). All five of them are based on the same general principle of PES discussed in Chapter 3 with the difference of studying different phenomena following X-ray irradiation. It is also possible to perform the so-called X-ray Absorption Spectroscopy (XAS)/ Near-Edge X-ray Absorption Fine Structure Spectroscopy (NEXAFS), which is a technique not used in the current experiments.

4.2.1 Optical Setup and Elements

During the earlier part of my Master work, the FlexPES beam was at the stage of its commissioning finalizing. Thus, it has been possible to follow and participate in multiple procedures which such commissioning included. The beamline was designed according to the so-called collimated optical scheme in which the photon beam coming out from the undulator is made straight and parallel by the optics.

The optics assembly of the FlexPES beamline can be seen below in Figure 4.3. The beamline has two branches, each with its own experimental station. There are two M3 mirrors, one for each branch, which can be positioned so that the photon beam is reflected into the corresponding branch. The branch used in the activities of the present work is the so-called B-branch (Fig.4.3).
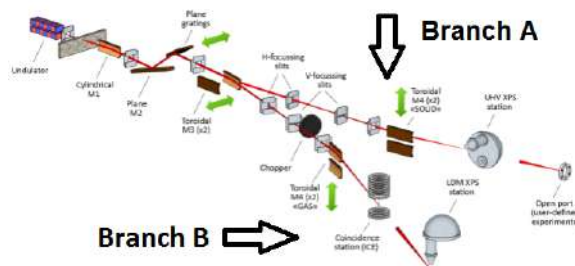
Figure 4.3: *The optical setup for the FlexPES beamline with all the individual optics elements. After the M3 mirror the beam can be directed into one of the two branches of the beamline - branch A to the right, and branch B to the left in the figure.*

As mentioned above, the beamline configuration is critical for delivering high-resolution and high-flux radiation to the sample under investigation. Together with the undulator, the beamline design also determines the photon-energy region and thus the energy levels that can be probed in atoms, molecules, clusters, liquids, and solids, as well as the spectral features which can be resolved. The beamline elements are a finely aligned system incorporating two mirrors M1 and M4, and a monochromator with two mirrors of its own (M2 and M3) and a diffraction grating (Fig.4.3).

4.2.2 Resolution and Resolving Power

One mandatory activity for any new beamline, especially the one meant for soft X-ray Spectroscopy, is determining the photon-energy resolution of the beamline through a series of measurements. This procedure was also implemented for the FlexPES beamline, branch B (seen in 4.3), and was carried out collectively with several people of the beamline staff and myself involved. To characterize the spectral resolution in different photon-energy regions, the recordings of the photon-energy dependent ionization efficiency of several gases – Helium, Nitrogen, and Neon were taken. For this purpose, the gases were let into a specially designed gas cell positioned in the B-branch after the monochromator (Fig.4.3). It is the monochromator which makes the most important contribution to the spectral width of the radiation reaching the sample. This width depends on the dispersion of the grating and the exit slit which physical opening can be varied.

It is important for the beamline personnel and users to know the resolution of the beamline for different conditions such as different photon energies and the monochro-

mator exit slit, as this can serve as a guide to designing experiments. It is also necessary to compare the experimentally measured resolution with that calculated in the beamline design process, as well as with other similar beamlines in the synchrotron labs around the world. The beamline configuration and optical schemes can be different at different facilities, and the resolution of a beamline is a measure of design and construction quality.

The team at FlexPes calibrated the photon-energy resolution by taking measurements with the beam that passed all optical elements except for the last refocusing M4 mirror (see optical scheme, Figure 4.3) and then went through the gas cell. As mentioned above, the gas cell contained one of the gases- He, N_2, or Ne. The gas cell is equipped with two electrodes: an anode and a cathode, that respectfully captures electrons and ions created by photo-ionization. With the help of a sensitive electrometer, we can get the electric current proportional to the number of ions/electrons collected by the electrodes. In figure 4.4 below a schematic illustration of how the gas cell looks like and operates can be seen.
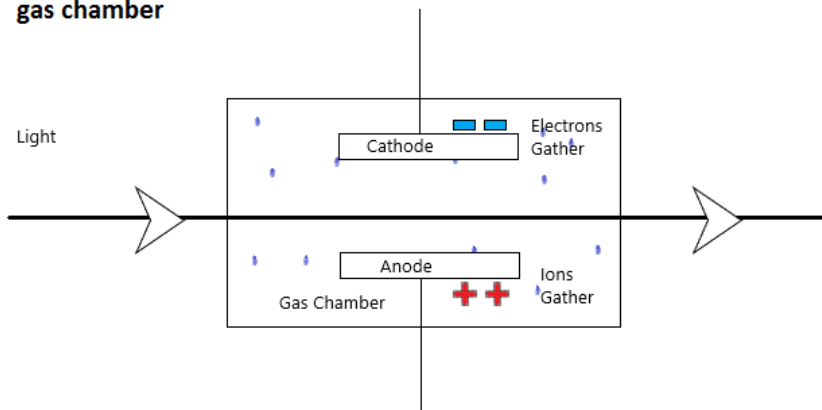
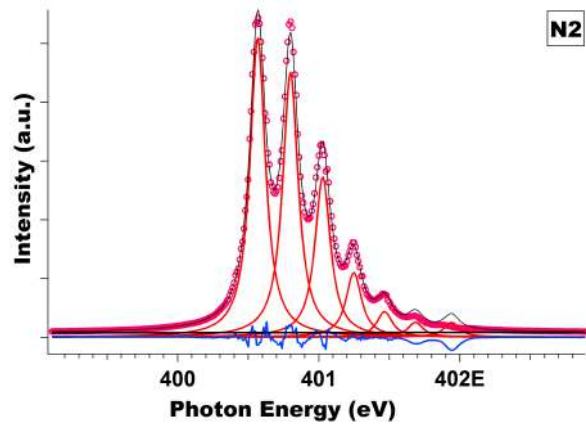**Figure 4.4:** *A schematic representation of the gas cell design and operation*

The slit cuts out a certain spectral interval from the spectrally dispersed by the grating X-ray beam. For the highest resolution, when recording the spectra presented below, we had a slit opening of 10 micrometers. The optical elements influencing the resolution are the M1 pre-optics mirror, the M2 plane mirror, the monochromator Grating (which works in unison with the undulator), the M3 toroidal mirror, and the exit slit.

The resolution is also defined by the source cross-section of the electron beam (usually denoted as the electron-beam size) and the chosen by the monochromator photon energy value. All these have been used by the beamline designers when they calculated the resolution of the FlexPES beamline. The resolution can be characterized in two ways: 1) by an absolute spectral interval which is cut by the exit slit at a certain photon energy; and 2) by a ratio of this photon energy to the spectral interval, which will give us the resolving power.
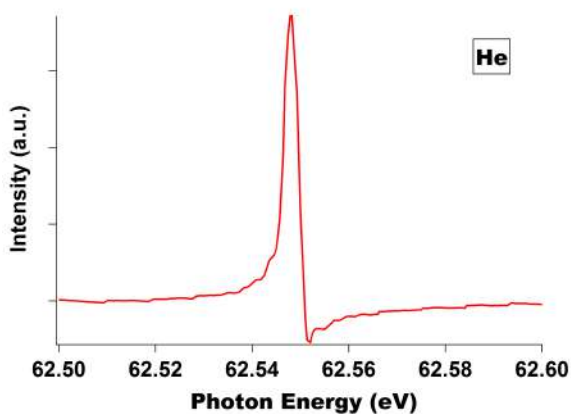
The procedure for recording the ionization efficiency of the gases is as follows. The monochromator scans the photon energy within the region of interest, where this or the other gas has its X-ray absorption region. The monochromator moves step-wise, stops at chosen intervals, then the undulator gap is optimized at each stop for producing the highest flux, and then the electrometer measures the current for a given time. Then the motion resumes. What is recorded is the so-called X-ray absorption spectrum, usually

containing "lines" corresponding to certain transitions in the gas under the irradiation. These lines have their natural spectral width described by a Lorentzian profile, but they are also broadened by the spectral width of the radiation interval defined by the optical settings, like the monochromator slit. This broadening is described by a Gaussian profile. One can fit the spectral lines and extract the latter broadening. This will be the absolute resolution. The fitting process for the spectra recorded was done with Igor Pro.

Figure 4.5 illustrates the fitting results for the Nitrogen 1s X-ray absorption spectrum. It was however the case that the Helium and Neon spectra had irregular steps when acquired in the measurements. That fact that made fitting by a standard Igor routine (which demands regular steps) so far problematic. It was however possible to separate the Lorentzian and Gaussian contributions to the spectral profiles for these two and thus estimate the resolution and resolving power.

Figure 4.5: *The fitted X-ray absorption spectrum for Nitrogen in the region N 1s. The core excited state* $1s^{-1}$ π^* *with different vibrational levels is the result of absorption.*

Further below, the figures are representing the X-ray absorption spectrum of He and Ne. Figure 4.5 contains the fitted absorption spectra for Nitrogen with several visible vibrational states of the pi* excited molecular state. It is known from the previous works on N_2 [42] that the Lorentzian-profile width of each vibrational "line" is 129 meV, which is the inverse of the lifetime of the core-excited state. From this value, the estimated resolving power is around 25000 while the calculated value was almost twice worse -around 15000.

(a) *The X-ray absorption spectrum for Helium with one of the autoinisation states of double-excited Helium. The energy-scale as recorded.*
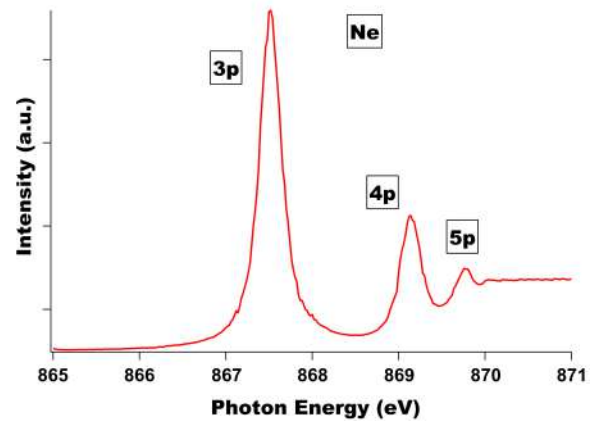
(b) *The X-ray absorption spectrum for Neon with the peaks corresponding to the* $1s^{-1}$*-> 3p,4p and 5p transitions starting from the left to the right*

Figure 4.6: *X-ray absorption spectrum for Neon and Helium that gives the profile contribution necessary for determining resolution power*

The discrepancy between the measured and the calculated value may depend on the Lorentzian width used. In some works, the width of 115 meV is given which leads

to a Gaussian profile of 63 meV and thus to the resolving power of twice worse than the calculated: 6300. The reality is probably the average of the two values which is then close to 15000, and thus to the calculated one from the beamline design parameters.

The resolving power of 15000 is a substantial improvement in comparison to the spectroscopy beamlines of the old Max-lab (such as I411 beamline) which had smaller values around 400 eV photon energy.[43]. In Figure 4.6a and 4.6b , the X-ray absorption spectra for Helium and Neon are presented, respectively, where I derived the FWHM from the spectra by procedurally measuring the distance between the points in the graph as the fitting was so problematic.

The experimental spectral width or FWHM that contains both the Gaussian and Lorentzian was found for Neon to be 315 meV. The convolution of the two profiles –the Lorentzian and the Gaussian- are known as the Voigt profile. The width of the Voight profile is connected with:

$$\Delta E_{Voigt} \approx \Delta E_{Lorentzian}/2 * \sqrt{\Delta E^2_{Lorentzian}/4 + \Delta E^2_{Gaussian}} \qquad (4.1)$$

and the Lorentzian profile for Neon was found to be 250 meV from literature. The resulting value for Gaussian is $\approx$ 190 meV, which corresponds to a resolving power of 4000 experimentally. For the helium transition, there is a narrow Lorentzian profile, practically zero, which means that the main contribution is the Gaussian from the beamline. The FWHM is $\approx$ 5meV in the spectrum and the resolving power for that experimentally is 12000, which is a bit lower than calculated, but can be influenced by uncertainty in the experimentally determined 5 meV width.
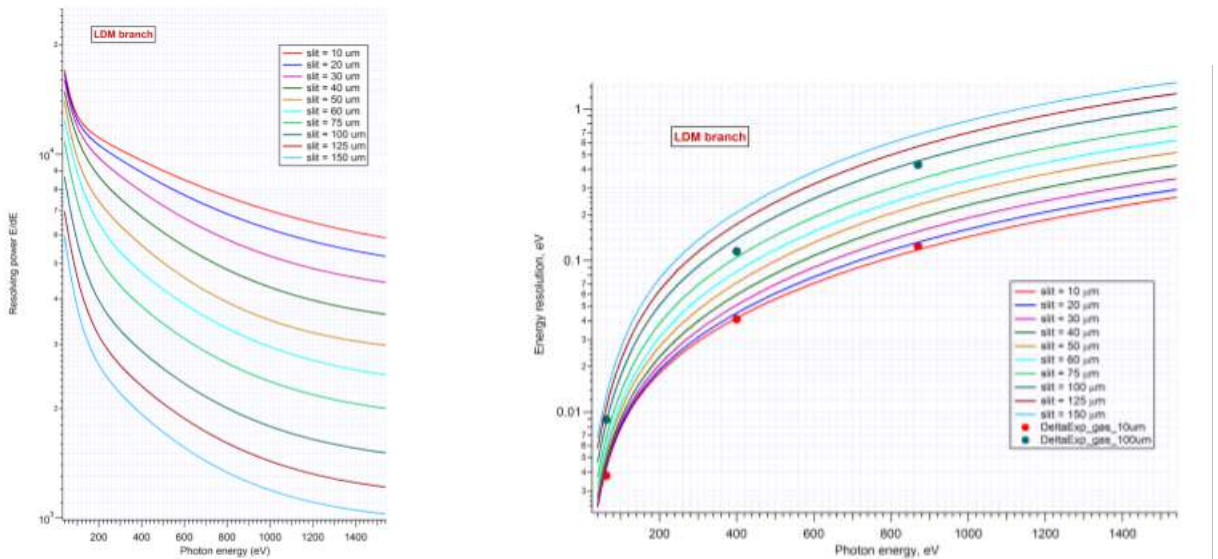

(a) The calculated Resolving Power for different exit slit sizes and photon energies for the B- Branch

(b) Calculated values for the Resolution, for different exit slits and photon energies for the B- Branch.

Figure 4.7: *Calculated values for the Resolving power and Resolution, for different exit slits and photon energies.*

In Figures 4.7b, 4.7a, there are some calculated values for the resolution and the resolving power for different exit slits and photon energies, courtesy of the FlexPES beamline manager Alexei Preobrajenski.

4.2.3 User Control and the GUI Interface

A characteristic feature of the beamlines at the new MAX IV synchrotron facility is a very high degree of automation and computerization. All elements of the beamline are steered via a graphical user interface, the synoptics of which is presented in Fig.4.8. We can see the individual valves, pressure gauges, slits and all their parameters on the
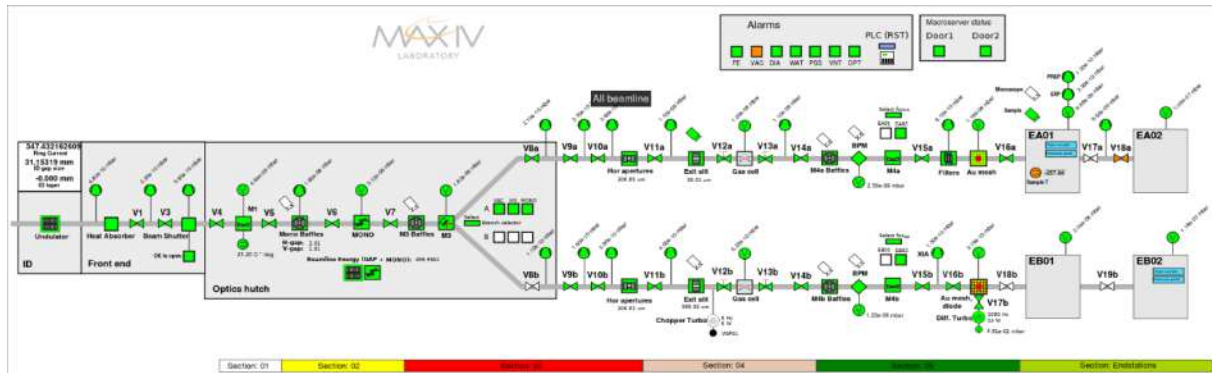
Figure 4.8: *The Beamline Graphical User Interface (GUI) which users need to control the machine and set parameters of operation for individual parts.*

screen. When users want to change something, they click on it and a window appears with the properties of the part and what can be changed. All parts are interactive including the undulator and monochromator, and users can select photon energies and beam characteristics this way. In the middle of the synoptics, is the M3 mirror, which is responsible for switching the radiation direction from branch A to branch B of the FlexPES beamline.

4.2.4 The Multipurpose End-Station

The branch B endstation, used in the described in this work experiments, is one of the four endstations of the whole beamline and is referred to as number 2 endstation and further on named PES endstation. (There is another, so-called ICE endstation at FlexPES branch B). The main tool of the PES endstation for the angle-resolved electron-spectroscopy experiments is the Scienta R4000 electron spectrometer. The details of this spectrometer operation will be explained in the next section. The whole arrangement facilitates experiments on gases, liquids, free clusters and solids. This end station has been partly relocated from the MAX-lab beamline I411[43].

The experimental station at FlexPes is a unique engineering solution allowing the rotation of the electron spectrometer around the light direction without breaking vacuum in the spectrometer. This is necessary to be able to detect electrons emitted at different angles. The radiation at FlexPes is linearly polarised in the horizontal plane. Electrons emitted from the sample tend to fly along the electric vector of the radiation which is horizontal. The angular dependence of the electron emission angle is known as the angular anisotropy of the photo-ionization process. To be able to rotate the spectrometer without breaking vacuum gives important advantages. There is a theoretical description of photo-ionization anisotropy, and an electron spectrometer which can measure electrons emitted at different angles can be used to test the theoretical predictions. However, the main advantage is probably that the spectrometer can be operated at the so-called magic angle of $54, 7°$. The purpose of this setting will be described in

24

the Appendix. Apart from the electron spectrometer mounted on the ionisation chamber the experimental station at FlexPes incorporates two other chambers: The so-called preparation chamber and the introduction chamber. These two chambers make it possible to introduce samples into vacuum without breaking vacuum in the ionization chamber.

The spectrometer chamber is pumped separately by two turbo pumps and two fore-vacuum pumps that are connected to corresponding controllers positioned in the control cabinet. The turbo pumps are separated from the spectrometer chamber by two gate valves. It is important, when this chamber is vented, to note the pressure and operating speeds of the pumps so the equipment is not damaged. The operating speed for the turbo pumps would be 60000 rpm/s and a current of 0.2A in the absence of any gas load. When we see a larger current on the display, it is an indication that the pump is trying to compensate for a leak or it is just starting up.

4.2.5 The Scienta R4000 Electron Spectrometer

The Scienta R4000 Electron Spectrometer was developed by an Uppsala company called GAMMADATA-SCIENTA, a spin-off of the Department of Physics at Uppsala University. The spectrometer is based on the electrostatic field property to deflect electrons. The field in the spectrometer is spherical and is created by two hemispherical electrodes. This is why the spectrometer is called an electrostatic hemispherical energy analyser. Ejected from the sample, electrons enter the volume between the electrodes at their one side, and the electron detector is on the opposite side. With a certain voltage on the electrodes only those electrons which have a definite kinetic energy pass all the way to the detector. This energy is called pass energy in the spectrometer acquisition system. The detector consists of two microchannel plates (MCP) and a glass plate covered with phosphorus. The microchannel plates are semiconductor devices which multiply the electron signal. Each plate increases the signal by a factor of one thousand. After being multiplied 1000x1000=1000000 times by the two MCPs the signal from each electron produces a light spot on the phosphorus plate. A digital camera is looking at this plate and records the light spots (electrons). The electrons with different kinetic energies are imaged at different parts of the detector, or, in other words, the electron signal is dispersed along the detector according to the kinetic energies of the electrons. The camera has 1024 channels, each corresponding to a certain kinetic energy value and a certain energy interval. This allows for detecting an electron energy spectrum. The camera is connected to the acquisition computer via the Ethernet interface/cable

As mentioned above, the spectrometer utilizes the physical principle that a spherical electrostatic field forces electrons to move along a circular trajectory, and only the electrons with a definite "pass" energy reach the detector for a given voltage on the electrodes. The spectrometer is operated at a set of predefined pass energies E_{pass} (ex. 20 eV, 50 eV, 100 eV, 200 eV, 500 eV), which are the electron kinetic energies the spectrometer works with.

The spectrometer has a detection energy spread of $\pm 5\%$: The electrons within the energy range of E_{pass} $\pm 5\%$ range - will have such orbits between the hemispheres that they will hit the detector. All other electrons will miss it. The pass energy E_{pass} is the value with which the electrons land in the middle of the detector. Then the whole

Figure 4.9: The Scienta 4000 energy analyzer as seen externally

detector can "see" 10% of the pass energy E_{pass} . Another crucial part of the spectrometer is the accelerating electrostatic lenses that see to the electrons speeding up or slowing down to the chosen pass energy. The voltages on the lenses are steered by the hardware in a power-supply rack and by a dedicated computer program. The kinetic energy of the electron is equal to the photon energy minus the binding energy for a specific level, as described in Einstein's photoelectric equation. Knowing approximately
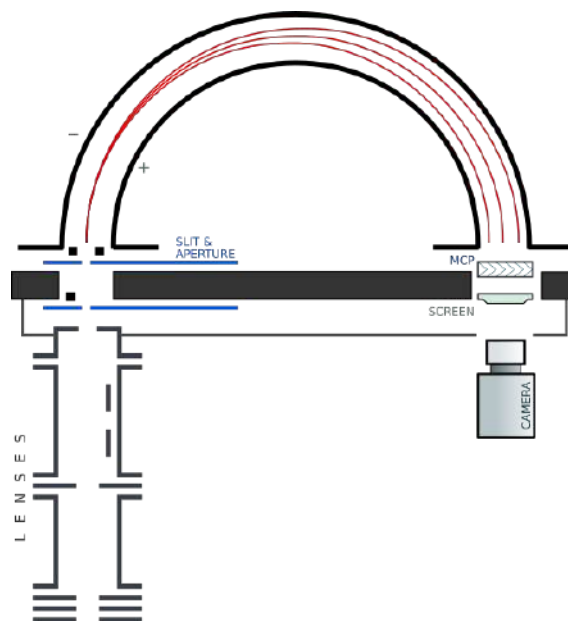
Figure 4.10: A principal of operation for any hemispherical electron analyzer like Scienta 4000 with the electrostatic lenses, slit and aperture carousel, hemispheres, microchannel plate, phosphorescent screen, and CCD camera.

the binding energy range of the energy level to be studied, one can configure the measurement in the Spectrometer software to get the kinetic energy range for which we want to have the detection. Both the kinetic energy range and the pass energy are important for a spectrometer as they will determine the energy resolution and the collection efficiency. For example, if we choose 500 eV for pass energy, then the energy range projected on the detector will be 10% of the pass energy: 50 eV. That would give us $50/1000 = 0,05$ eV/channel of the CCD camera, while 200 eV pass energy gives 0,02 eV/channel. Therefore with smaller pass energies one gets better resolution, but

loses in detection efficiency. There are 2 modes of operating the spectrometer. The ''Fixed'' mode (what was described) and the ''Swept'' mode, which briefly speaking, sweeps the energy interval that will be imaged on the detector, so a wider than 10% of the E_{pass} can be recorded in one-electron energy spectrum. Apart from the pass energy, also the spectrometer entrance slit size and shape influence the energy resolution in a spectrum.

As mentioned above the operation of the Spectrometer happens under the ''magic angle'' $\theta = 54,7°$, at which one places the photoelectron detection direction relative to the horizontal polarization plane of the X-ray radiation. The purpose of that is to maximise the detected signal and minimise the role of the photo-ionization anisotropy. (see Appendix)

5. The Experiments on Clusters at FlexPES

In this Chapter, our own experiments on clusters will be presented.

The results of the water cluster experiments have not brought any surprises: the correlation between the secondary electron production and the primary photoelectrons has been established and quantified. In the experiments with metal nanoparticles, we succeeded for the first time detecting silver oxide response of the clusters in the Ag 3d range, earlier it was done only in the valence region.[28, 31]. Some results on the silver oxides were unexpected: as described above, current literature seems to not have reached a consensus on the binding energies and spectral shape of the silver oxide response in the Ag 3d region, and our data occurred to be adding more grounds for further discussions.

5.1   Experiments on Water Clusters at FlexPES

As described in Chapter 2, the experiments on water clusters were performed using an adiabatic-expansion cluster source producing a cluster jet as a result of rapid cooling leading to clustering conditions. The probing technique used was XPS following the ionization of the clusters by the intersecting synchrotron radiation. Due to the new demands of the oil-free vacuum at MAX-IV, as well as the prohibition of using equipment from the old Max-lab, a new adiabatic-expansion source was designed and its components were ordered and manufactured. I took part in assembling the new cluster apparatus, performing off-line commissioning tests, and the first experiments at FlexPES beamline, the results of which will be presented below.

5.1.1   Overview of Water Cluster Experiments

As described in detail in Chapter 2, the new cluster source comprised a dedicated vacuum chamber, a pumping system, and an XYZ manipulator, the latter enabling the movement of the water container with the nozzle. This setup that combined several different working parts was attached to the ionization chamber of the FlexPES endstation.

Using the Z-motion of the manipulator we could move in or retract the water container in or out of the ionization chamber while using the XY-motion of the manipulator we could adjust the cluster beam position relative to the photon beam. The ionisation chamber was connected with the cluster source only through a 500-micron orifice skimmer(Fig 2.1), which enabled high vacuum to be held in the ionization volume and in the spectrometer. In the current experiments, we had occasions where blockages of the nozzle were encountered or disconnections in the wiring, and these problems had to be addressed as they can lead to long times when the setup operation or/and measurements were not possible.

To optimize the alignment, we had to rely on the detection count rate from the spectrometer —meaning trying to catch the maximum amount of electrons. As was mentioned in Chapter 4, the X-ray beam in this beamline has the dimensions of 120x100 micrometers at the focal point opposite to the spectrometer entrance. As also described in Chapter 4, the spectrometer has a small volume of detection and a narrow detection
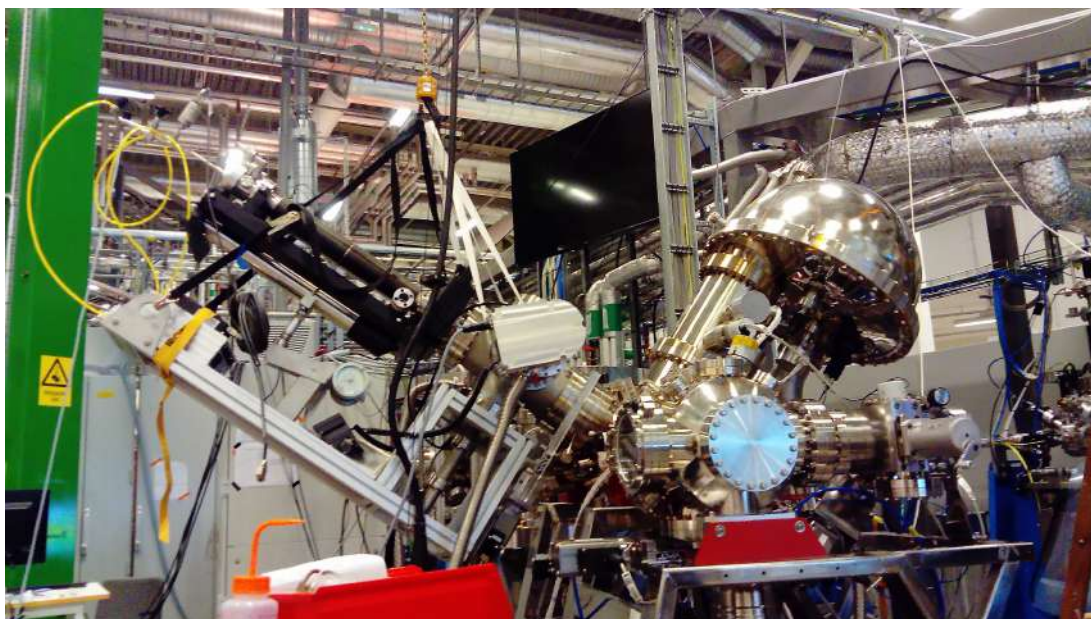
Figure 5.1: *The whole setup, mounted at an angle with the Scienta-spectrometer chamber. The manipulator that contains the water cluster source is seen in the middle supported by the crane*

angle. It is critical for the signal detection to have the best possible overlap of these three areas: of the spectrometer detection volume, of the X-ray beam, and of the cluster beam.

The procedure of the cluster source operation was as follows. We checked for leaks after mounting each extra component and followed a certain sequence of actions while starting pumping. Otherwise, some components like, for example, gate valves can be destroyed. When the oven was charged with water it was moved forward to come close to the skimmer, then the heating was turned on, the temperature rose slowly leading to the gradual rise of the vapour pressure, and the vapour expansion into vacuum created the cluster beam.

The valence levels were ionized with different photon energies, thus producing photoelectrons with different kinetic energies. In general the faster the electrons are, the more secondary electrons they can produce on their way through the clusters towards outside. These secondary electrons are produced by so-called electron-impact ionization. Each such ionization event of a constituent molecule inside the cluster demands around 10 eV quantum of energy. If initially, the photoelectrons have several times this energy, they can ionize a corresponding amount of molecules on their way out.

Recently, another efficient mechanism of ionization in water clusters has been suggested- the so-called Interatomic Coulombic Decay [44]. The ionization of the 2s inner valence level of water clusters leads to the Auger-like process: the inner-valence vacancy gets refilled, but the released energy goes not to the ejection of an electron from the same molecule (like in the Auger), but from the neighbouring one. In separate molecules, this process is not possible because of the absence of neighbours, so the released energy is taken away by a photon.

5.1.2 Operational Conditions, Procedures and Data Acquisition

Several details must be considered when conducting the water-cluster experiment. Extra care must be taken to find balanced conditions for reaching an acceptable vacuum without wasting time. Exposing the fore-vacuum pumps to water vapour is also a danger, so the use of liquid nitrogen cool traps in the vacuum lines from the turbo pumps to the fore-vacuum pumps was necessary - to catch the water vapour.

On the side of the endstation opposite to the cluster source, we installed a dedicated cool trap for catching and freezing the water jet (Figure 5.2). All the cool traps were regularly filled with liquid nitrogen. The traps work as efficient pumps for water vapour, so it also improves vacuum in all chambers.

Figure 5.2: The backside of the Scienta-spectrometer chamber, where the cluster beam was caught with a mounted cool trap filled with liquid nitrogen.

When everything was ready, we tried to get some electron signal from the clusters using the Scienta- spectrometer. To optimize the signal from the cluster jet, the mirrors and the monochromator of the beamline had to be tuned. As mentioned in Chapter 4, this is possible to do from the main control program of the beamline in the "hutch" using the GUI interface.

Having the cluster size estimation for different conditions (described in Chapter 1), it was clear where the nominal conditions for this experiment would lay. Therefore the goal was to reach the water vapour pressures of about 3 bars and about 6 bars in the oven aiming at the cluster size of around 1000 molecules and 3000 molecules per cluster correspondingly.

These pressures were calculated using the approach and results of Bobbert et al. [4], as discussed above. For a range of pressures, the expected cluster sizes are presented in Figure 5.3.

For each of the two sizes (1000 and 3000 molecules/cluster), the measurements were taken at a series of photon energies increasing the photon energy until we could still have detectable signals. In one series of measurements after some time of operation, there was a pressure gauge failing, so we had to rely on the vapour-vs-temperature tables using the controlled temperature of the oven. Our beam time lasted for two days, which was enough to obtain the data that we wanted.

5.1.3 Spectral Analysis, Results, and Discussion

In the initial tests and measurements in both the valence region and O 1s core-level region, the presence of the water cluster signal was established. As mentioned in Chapter 2, uncondensed water molecules are also present in the cluster-containing jet, so, apart from the cluster signal, there is also the signal from the water molecules in both spectra (Figs.5.4 and 5.5). The molecular signal is well studied, so it was used for the binding energy calibration in our experiments. Our observations agreed well with the previous results found in literature. [46]

Pressure in Bars	Pressure in Pa	Temperature in Celsius	Temperature in Kelvin	Cluster Size \<n\>	Pressure in Bars	Pressure in Pa	Temperature in Celsius	Temperature in Kelvin	Cluster Size \<n\>
1,0	100000	99,6	373	119	4,0	400000	143,6	417	1318
1,5	150000	111,4	385	241	4,5	450000	147,9	421	1615
2,0	200000	120,2	394	398	5,0	500000	151,8	425	1936
2,5	250000	127,4	401	586	5,5	550000	155,5	429	2280
3,0	300000	133,5	407	803	6,0	600000	158,8	432	2647
3,5	350000	138,9	412	1047	6,5	650000	163,4	437	2980

Figure 5.3: *The resulting cluster sizes for different operation parameters, the dimensions and various conditions. The calculation for the necessary temperatures was made using water vapour calculators and tables[45]*

In Figure 5.4 one can see a typical spectrum recorded in the valence-level energy region at 43 eV photon energy. The spectrum is presented on the kinetic energy scale. The photon energy was chosen from the consideration of getting around close to 32 eV kinetic energy for the cluster photoelectrons from the X state. This is the lowest kinetic energy possible to reach at FlexPES for the water X-state, so this is the starting point for a series of measurements taken at different photon energies. In Figure 5.4 at 30.5eV, the spectral features due to the vibrational level ionization of the X molecular state are visible. The other "bumps" in between 29 and 25 eV are the overlap of clusters' and molecular water signals of the a and b states.
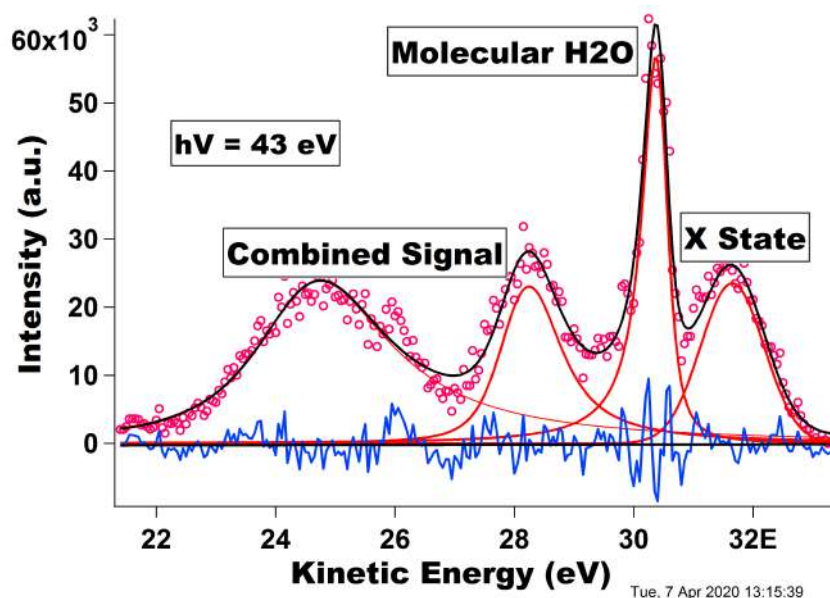
Figure 5.4: *A typical valence spectrum, here recorded at 43 eV photon energy. The average cluster size is 1000 molecules. The first from the right peak is attributed to only water clusters, the second from the right sharp peak to molecular water and finally the rest two peaks at lower kinetic energies are overlapping cluster and molecular signals from the a and b states.*

Below in Figure 5.5 an example of a fitted experimental spectrum acquired for the ionization of Oxygen 1s state in water clusters and uncondensed molecules in the jet recorded at 600 eV photon energies can be seen. The pass energy used for record-

31

ing this spectrum was 100 eV, giving about 0.13 eV instrumental contribution. The monochromator slit spectral width was 0.14 eV.
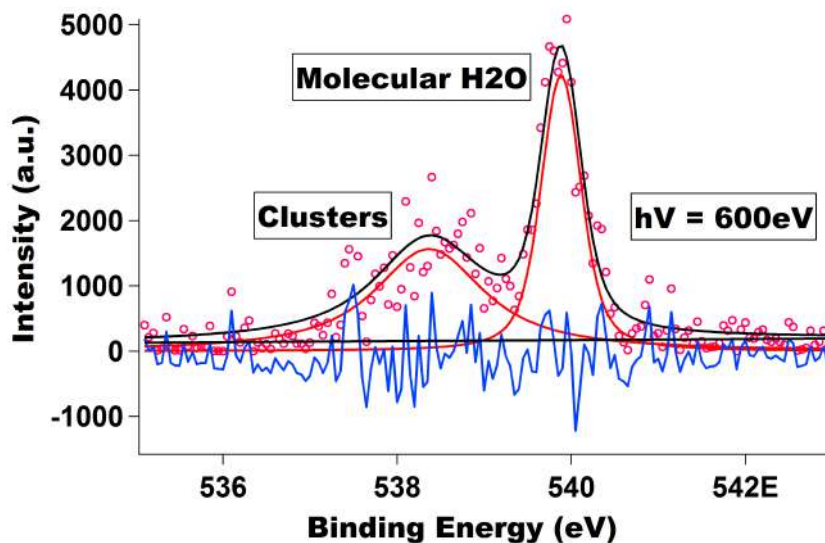
Figure 5.5: *A typical O 1s spectrum from a beam containing water clusters and molecules, recorded at 600 eV photon energy. The average cluster size is ≈1000 molecules. The red hollow circles are the experimental data. There are two "peaks" in the spectrum. The narrow peak is the molecular water and the broad peak is due to the ionisation of the water clusters. The red lines are the fits for the individual peaks, and the black line is the sum of the fits for the individual peaks. The blue line is the deviation between the experiment and the fitting*

In the analysis, I had to quantify the cluster signal, and for that I chose the well-separated cluster feature centered at 32eV which is, as mentioned above, due to the ionized cluster peak of the X-state. This feature area, which is proportional to the cluster intensity, could be obtained by fitting it using the Igor Pro software package. As discussed in Section 5.1.1, the goal was to measure the valence spectra at different photon energies, quantify the cluster signal, and compare it to the secondary-electron signal, also recorded at each photon energy used for the valence spectra. The valence- and the secondary- electron spectra were recorded using a 50 eV pass energy of the spectrometer giving ≈ 0.06 eV instrumental broadening. The monochromator slit was chosen correspondingly at each photon energy to match this value. Below in Fig.5.6 and Fig 5.7 the experimental data for the cluster size 1000 and 3000 molecules/cluster, respectively, for different photon energies can be seen.

These spectra constitute and document the main experimental results of the part where the water clusters were studied, and they are the basis for the analysis performed and conclusions made. The left panel in both figures presents the valence spectra, and the right panel- that of the secondary electrons. As can be seen from the signal-to-noise ratio in the valence spectra, the intensity went down with the photon energy. There are several reasons for that: 1) the decrease of the ionisation probability of the oxygen 2p level (which is the main contribution to the water molecular orbitals here) with the photon energy; 2) the decrease of the beamline flux above 100 eV photon energy, and 3) the necessity to close the monochromator slit with the photon energy in order to preserve the same spectral resolution. As mentioned above, due to technical problems, the secondary-electron spectra for 1000 molecules and for 3000 molecules were detected in different kinetic energy intervals, while in reality, they appear in the same regions. The exact limits of the region may have deviated from those shown

in Figures 5.6 and 5.7, however, the intensity can be trusted. The above-mentioned technical problems lead to the fact that the cutoff of the secondary-electron signal is observed at around 4 eV in the spectra for 1000 molecules, and at around 8 eV for the case of 3000 molecules. In reality, the kinetic energies were the same, so the conclusions made and discussed above were not influenced. It should be also mentioned here, that one should not attribute any meaning to the shape of the secondary-electron spectra, in view of the imaging problems of the spectrometer in the low-energy region. The electrons were detected at various parts of the detector and then integrated over the detector area, and that created the presented shape. And again that imperfect imaging should have influenced the electrons in the same way for each photon energy used, so the comparison between different cases is valid.

After obtaining the area I_v of the valence X-state cluster feature and the secondary electron signal I_s for two different clusters sizes of $\approx$1000 and $\approx$3000 molecules I calculated the ratio I_s / I_v for corresponding photon energies.

It should be added here that the sensitivity and imaging properties, known also as transmission function, of the Scienta hemispherical spectrometer, become poorly defined and change non-uniformly in the region of very low kinetic energies. In the long run, this influences the I_s / I_v ratio. While it is, in principle, possible to get a certain idea of the spectrometer transmission function in the low-kinetic-energy region, at the time of the described experiments certain technical difficulties did not allow doing it. Thus, the I_s intensity values of the secondary electrons were used as measured. The uncertainty is then transferred into the absolute I_s / I_v values. However, the experiments had first of all "a demonstration of principle" goal, and as discussed further down, more experiments are necessary to make the results quantitatively accurate.
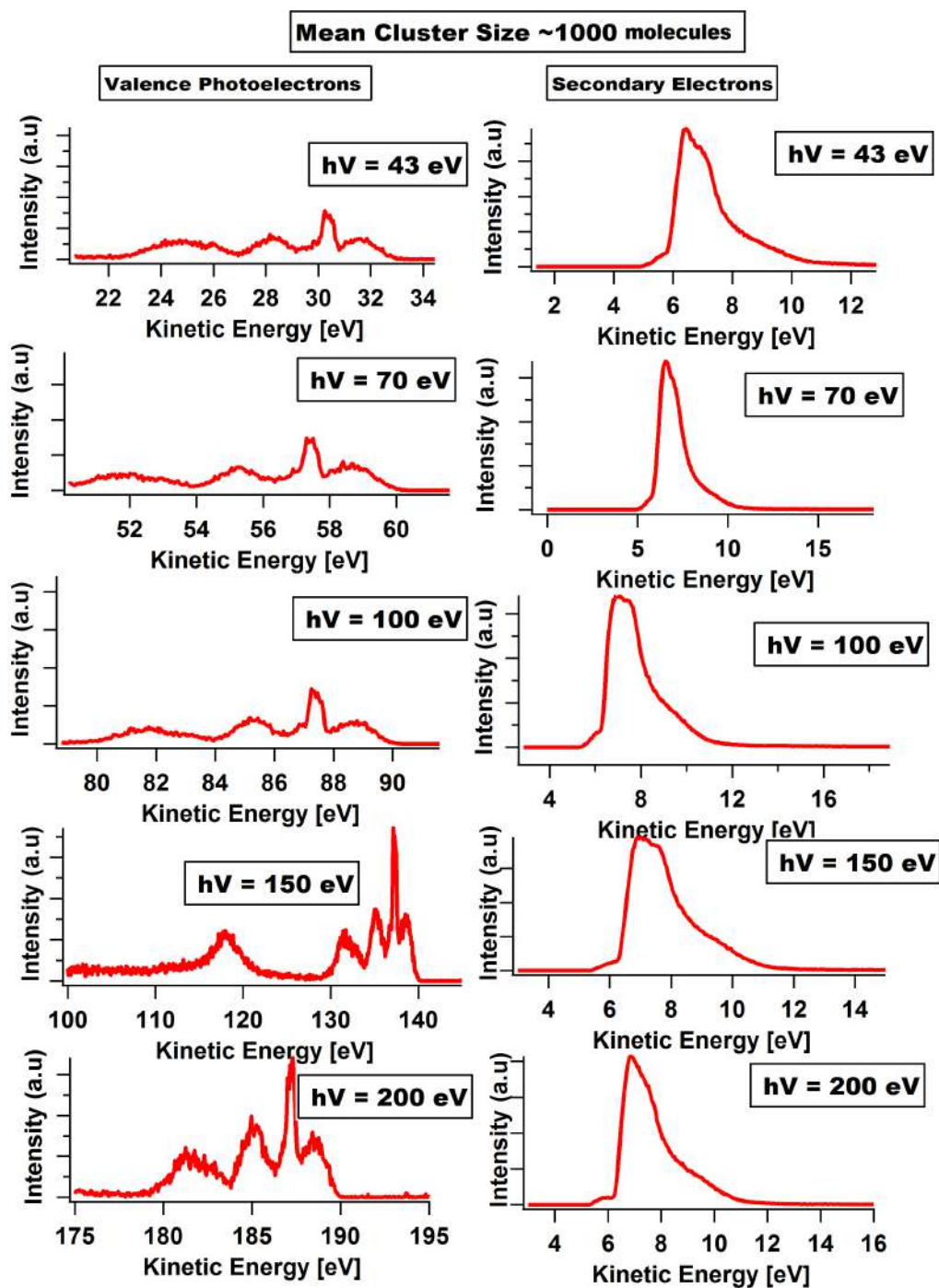
Figure 5.6: *Experimental data for the average cluster size of 1000 molecules/cluster. The valence- level spectra are shown in the left panel, and the spectra of the secondary electrons - in the right one.*
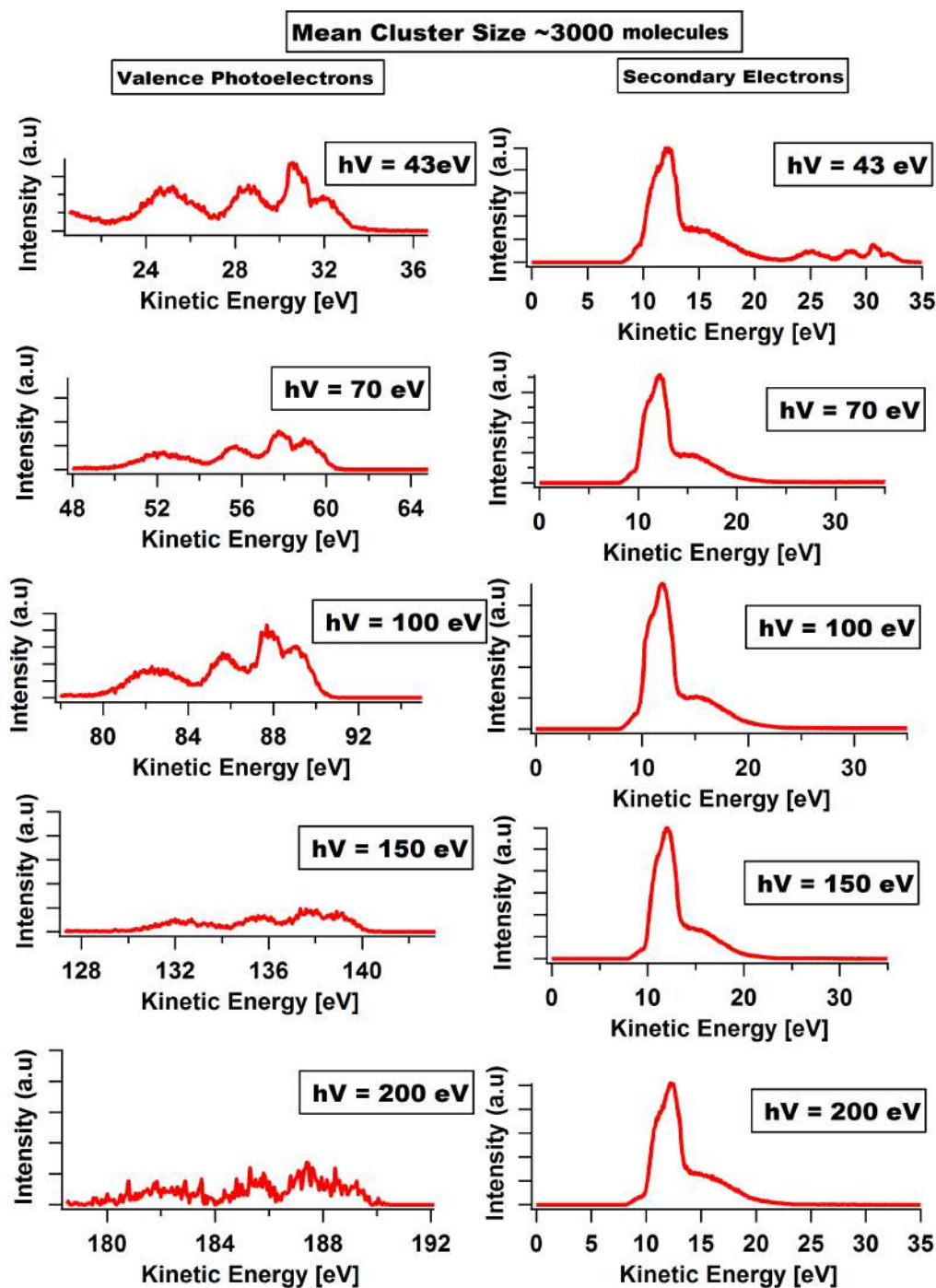
Figure 5.7: *Experimental data for the clusters of the average size 3000 molecules/cluster. The valence-level spectra are shown in the left panel, and the spectra of the secondary electrons - in the right one.*

The results of the spectral analysis are presented in Figure 5.8a for the mean cluster size of 1000 and in Figure 5.8b for the mean cluster size of 3000. As mentioned above, three different factors cause the decrease of the primary signal of the photoelectrons with the photon energy increase, and as a consequence, the secondary-electron signal also decreases.

From these results it is possible to make a judgement concerning what conditions produced the higher relative signal of the secondary electrons. There is a clear rising

trend of the relative production of secondary electrons as the photon energy, and thus the kinetic energy of the photoelectrons increases (Figures 5.9a and 5.9b). The photoelectrons with the higher kinetic energy can kick out more electrons from the valence level of the clusters - on their way out from the clusters.
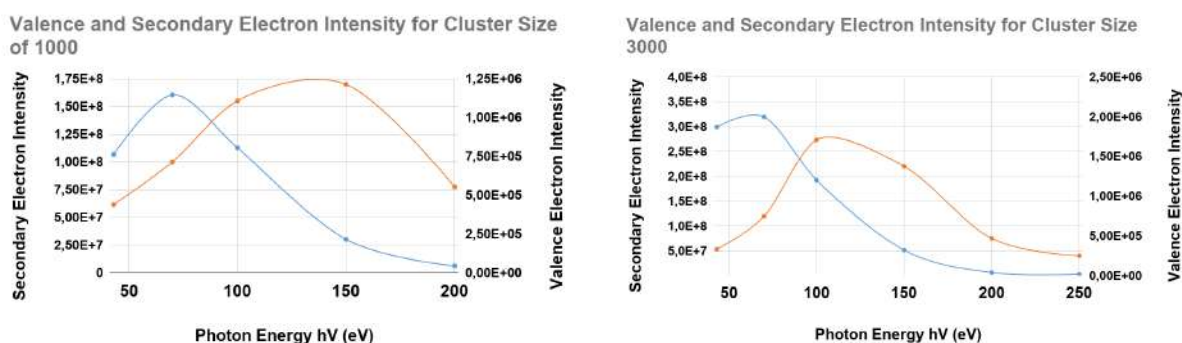
(a) *With blue the intensity for the valence signal I_v, and orange the secondary electron signal I_s. Mean cluster size of 1000 molecules.*

(b) *With blue intensity for the valence signal I_v, and orange the secondary electron signal I_s. Mean cluster size of 3000 molecules.*

Figure 5.8: *The results of the spectral analysis for the mean cluster size of 1000 and 3000 molecules/cluster for different kinetic energies. Blue – the signal I_v from the valence cluster electrons (X-state) quantified as the area under the corresponding spectral feature. Orange - the signal I_s estimated as the area under the secondary electron feature.*
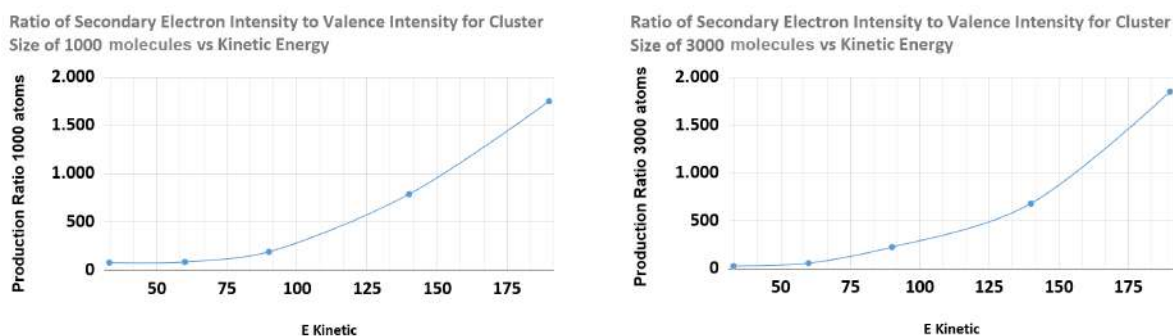
(a) *The secondary production ratio for a mean size of 1000 molecules/cluster*

(b) *The secondary production ratio for a mean size of 3000 molecules/cluster*

Figure 5.9: *The relative Is/Iv signal for different kinetic energies.*

5.2 Experiments on Silver & Silver-Oxide Clusters at FlexPES

The experiments on silver clusters were to a large extent inspired by similar experiments conducted at Max-Lab and were meant, among other goals, to test the capabilities of the new FlexPES beamline for the studies of free individual metal clusters in a beam. The described measurements were the first of its kind at the new FlexPES beamline, so one can consider these measurements to be also a commissioning of the refurbished metal-cluster source in junction with a new beamline. The equipment and instruments of the endstation and the beamline, to which the metal cluster was attached for the measurements, remained the same as in the water cluster experiment, only the skimmer was changed from a 0.5 mm to 2 mm diameter one. In the present ex-

periments it was possible to observe both the metallic and the oxide signals in the same spectrum. From earlier works, it is known that both signals come from the nanoparticles of a complex composition. [47]. This allowed us to have an internal reference for the calibration- the metallic "line" position.

5.2.1   Operational Conditions, Procedures and Data Acquisition

The main details of the magnetron- based nanoparticle source have been described above, so in this chapter, only the specific operational parameters will be described. The nanoparticle source was attached to the FlexPES- beamline experimental station and rotated to the magic angle of the spectrometer.

The power of the magnetron was stabilized at 200-250 Watts. The flow of Argon and Helium gas was set so that their input pressures were 7- 8 mbars. The oxygen bottle was connected to the same gas inlet as the argon. The oxygen pressure reached up to 30% of the total $Ag - O_2$ mixture. The measurements were done in the following way. First, the optimal conditions were found for producing metallic silver nanoparticles (with no oxygen admixed). This has been done by monitoring the valence-region signal of the particles in the real-time acquisition mode of the spectrometer.

The beamline energy was set to 60eV, and the monochromator slit corresponded to 0.15 eV spectral width. Figure 5.11(top panel) presents a typical valence spectrum of metallic nanoparticles with the 4d (from 8 to 12 eV) and 5s(from 4 to 8 eV) bands resembling those of the solid macroscopic silver. From the close to macroscopic value of the particle WF, the size of our metallic particles (Fig. 5.11, top) could be estimated to be around 10nm. This could be done using the conducting sphere approximation. Then the spectrometer and beamline parameters were changed for making it possible to record the Ag 3d signal.

For that, the binding energy range was set to 365-385 eV. The photon energy was set to 420 eV, with 0.4 eV spectral width of the monochromator slit. In the spectrometer the entrance slit had to be increased for letting more electrons in and thus getting a stronger signal. That made the spectrometer instrumental broadening to be ≈0.4 eV. A recorded at these conditions typical Ag 3d signal from the metallic nanoparticles, is presented in Figure 5.12(top panel). As in macroscopic silver metal[8], the signal is a spectroscopic doublet – due to the Ag $3d_{5/2}$ and Ag $3d_{3/2}$ final ionic states. What is different relative to the published spectra of microscopic silver is the absolute energy scale – defined relative to the vacuum in this case. For the spectra of microscopic metallic samples [48] it is the Fermi edge

Figure 5.10:   The Metal Cluster setup mounted at an angle to the Scienta-spectrometer chamber. The manipulator that contains the metal cluster source is seen in the middle.

(the onset of the metal valence band, the 5s band in the case of Ag) which is taken for the zero binding energy point. This is done because for the so-called "supported" samples, which are grounded, the vacuum level is difficult to establish in the spectrum. For the free particles in the beam, this is easy to do using the calibration provided by the co-existing in the beam argon and helium gases. To recalculate from the available

in literature binding energies E_B(Fermi) of the macroscopic silver to the binding energies E_B(vacuum) relative to the vacuum level one has to add the macroscopic-silver work-function WF to the core-level binding energy E_B(Fermi)[8]:
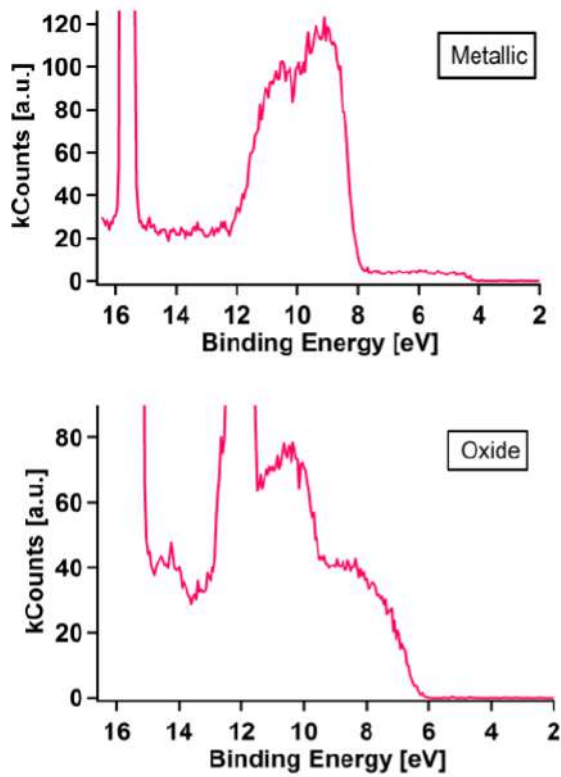
$$E_{Bvacuum} = E_{BFermi} + WF \qquad (5.1)$$

The silver work-function found in literature varies somewhat from publication to publication- due to the principal difficulty in the WF experimental determination. Nevertheless, when the averaged silver WF was added to E_B(Fermi) the resulting macroscopic Ag 3d binding energy occurred to be in the 0.1-0-2 eV vicinity to the binding energies of the free silver nanoparticles. This provides a further validation that the silver clusters produced are nanoscale pieces of solid silver having practically the same electronic energy levels as the macroscopic metal.[8]

After the metallic nanoparticles were characterized, we could proceed to produce and characterize the nanoparticles containing silver oxides. The previous experience [30] with the metal-cluster source in question suggested that the increase of the oxygen fraction in the argon-oxygen mixture would lead to the production of oxides with higher oxidation states.

In the previous work on silver-oxide nanoparticles [30] the highest fraction possible to reach was 20%. In the current work, we were able to reproduce the conditions of work [30] that the spectra presented in figure 5.11 bear a witness of. The top spectrum of metallic particles produced in the current work practically reproduces a typical valence spectrum of macroscopic polycrystalline silver. That serves as the ground for our conclusion about the metallic nature of our nanoparticles produced in the absence of oxygen in the sputtering mixture. The shape of the bottom spectrum in Figure 5.11, when compared to those silver oxide spectra

Figure 5.11: *Valence spectra recorded at 60 eV photon energy. Top spectrum, pure silver nanoparticles. Bottom, silver-oxide nano-particles with 20% oxygen admixed.*

from work [30] proves that a high oxidation degree of silver was reached in our nanoparticles already when 20% oxygen was admixed to argon.

In the case of gold-oxide nanoparticles [49], the oxygen fraction reached 30%. This range of oxygen fraction occurred to be the working range for the present experiments. Both valence (Fig.5.11 bottom) and Ag 3d core-level spectra were recorded for a series of O_2 fractions in argon, in particular for 20% and 30% (Fig.5.12 middle & bottom panel). With the oxide presence in the particles, a second Ag 3d doublet appears in the spectrum at binding energies higher than those of the metallic doublet. This situation has been typical, for example, in gold-oxide particles.[49] In these earlier studies

of metal-oxide nanoparticles the second doublet was interpreted as due to the metal atoms coordinated to oxygen in the particles, in other words - due to the metal oxide.

## 5.2.2 Spectral Analysis, Results, and Discussion

If one is to analyze the spectra containing a silver-oxide response, one has to first establish the spectral parameters for the metallic doublet- from the spectrum recorded at the conditions when no oxide is still formed (Fig.5.12top panel). This is necessary since the oxide-containing spectra also have the metallic doublet which one has to fit, but which has low intensity and is partly obscured by the oxide doublet. The metallic spectrum in Fig.5.12 top panel was fitted using the so-called Doniach-Sunjic asymmetric profile, typical for core-level lines in metals, in the assumption of the statistical $3/2$ intensity ratio of the spin-orbit components, 0.36 eV life-time-defined Loretzian widths [50], left-free Gaussian broadening, and a flat rising background. The described above parameters must be declared or left free in the fitting routine in the Igor program. There was no attempt made to assume the plasmon presence in the spectra. The spectrum was calibrated using Ar 2p lines showing up at around 250 eV. The results of the fitting are included in the spectrum itself as the constituent spectral "lines".

Then the oxide spectra recorded at 20% and 30% oxygen fractions in argon were calibrated with Ar 2p signal. This calibration allowed to reassure that the lower-energy doublet in them was due to the metallic component in the particles: it appeared at practically the same binding energy (within the experimental uncertainty) as in the pure-metallic spectrum (Fig.5.12b top panel).

As can be seen from figure 5.12, in the oxide spectra in the middle and at the bottom, the metal doublet is slightly shifted up in binding energy - for about 0.3 eV. This can be explained by the somewhat different long-range environment in which silver atoms get with the oxide appearance in the particles. Namely, when the particles are pure metallic, the probed silver atom sees only other silver-metal atoms at any distance. When the particle gets an oxide part, it likely constitutes the particle's inner part - the core, and the remaining metallic part makes a shell around the oxide core. Then silver atoms in this metallic shell see different long-range environments- namely, within a nanometre or less there can already be the oxide part or the interface with it. That creates somewhat different (relative to the pure metallic case) electronic configurations in the initial and in the final states, and thus somewhat different binding energy peak positions for the metallic doublet. The size of the oxide-containing particles could not be estimated using PES, however, in earlier works with the current setup it was possible to perform TEM on deposited from the beam metal-oxide particles created at similar conditions. The TEM image gave the size of 10 ± 5nm.

For the oxide doublet itself, the spin-orbit separation was taken equal to that in the metallic doublet, and also the Lorentzian widths used were the same, as well as the spin-orbit intensity ratio. The Gaussian widths demanded as a separate parameter by the fitting program for building the Voight profile (we used the Lorentzian widths fixed to 0.36 eV) of the Ag $3d_{5/2}$ and Ag $3d_{3/2}$ lines in the oxide doublet, were left free but equal to each other. The results of the fitting are presented in Fig.5.12a,(middle & bottom panel, left side), as constituent lines. In the middle spectrum (20% O_2 fraction) the separation between the metallic and the oxide doublet is 2.0±0.2eV. In the bottom spectrum (30% O_2 fraction), it is more like 2.5 eV, however, the noise level is too high

to make a reliable statement of a larger oxide shift in this case.
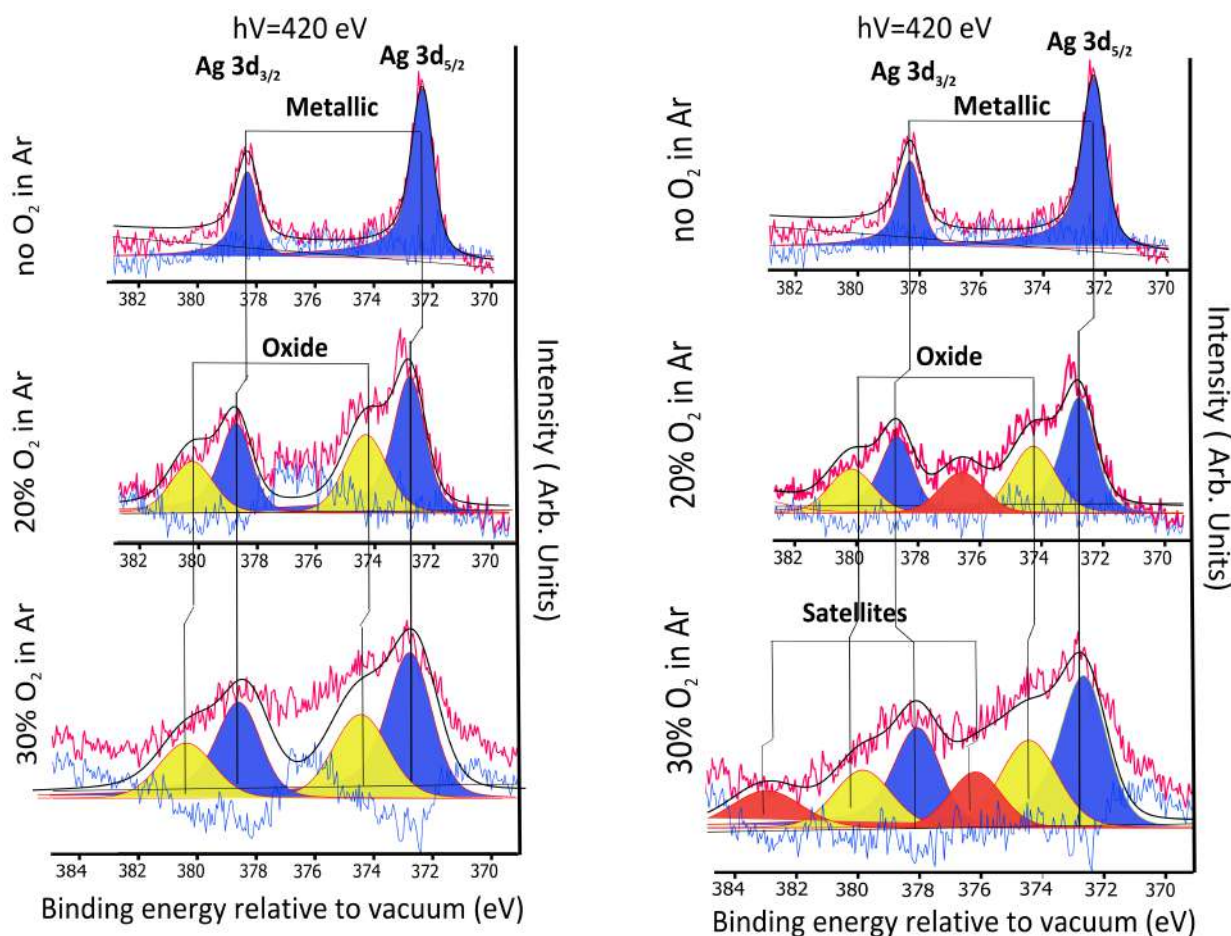
(a) *The results of the fitting made assuming no satellites.*

(b) *The results of the fitting made assuming satellites' presence.*

Figure 5.12: *Ag 3d region. The position of the metallic peaks (blue), the oxide peaks (yellow), and the satellite peaks (red, on the right) are marked with vertical lines.*

In (Fig.5.12a (middle & bottom panel, left side), we also see that the fits for the oxides have a small problem in between the Ag $3d_{5/2}$ and Ag $3d_{3/2}$ groups. The intensity there can be well fitted by an extra peak (Fig.5.12a middle & bottom panel, right side). This peak can be the satellites due to the opened valence 4d shell in the ground state of the oxide, which in [34] were calculated to appear in between the main Ag $3d_{5/2}$ and Ag $3d_{3/2}$ oxide lines. According to work [34] there should also be a satellite feature above the Ag $3d_{5/2}$ group in binding energy. And indeed, the fit becomes better if another extra peak is assumed to be present there (Fig.5.12b middle & bottom panel, right side).

Coming back to the value of the oxide shifts – 2.0 to 2.5 eV – detected by us in the spectra, one can note that these are positive shifts – in contrast to the earlier picture of negative shifts for both silver oxides. Besides, such a large oxide-shift value has not been observed before. At the same time, a 2-3 eV positive shift is rather typical for the metal oxides with higher oxidation states [16], so it is tempting to assign this observation as due to the AgO oxide. Below, in Table 5.1, one can observe the differences that

Types of Silver Oxides AgO	Oxide Shifts Found in Literature	Oxide Shift Range in Current Work
Ag(I)	-0.5eV	2-4 eV
Ag(II)	-	-
Ag(III)	-0.8eV	2-4 eV

Table 5.1: *Table showing the oxide shift differences found in literature and those found in the current work.*

exist in literature [31, 32, 35, 36] and in the present work in both sign and value for the oxide shifts. As discussed above, this oxide has silver with the oxidation state I and III, so in our nanoparticles, the relative abundance of these two silver-atom coordinations may change with the oxygen's fraction increase- towards the presence of more of the Ag(III)-oxide. However, at this stage, a definite conclusion is perhaps too early to make, and more efforts should be made to improve the signal-to-noise ratio and perhaps to try to deposit the particles, an approach that should create a higher nanoparticle concentration irradiated by the X-rays than in a dilute beam of free nanoparticles.

It cannot be excluded that at least a part of intensity ascribed to the satellites (red peaks in 5.12) is due the higher oxidation state Ag(III), and then the lower-energy doublet (yellow peaks) is due to the Ag(I)-oxide. One has to study it more. However, the shift for the red doublet is about 4 eV, which is a rather large shift. And then, if the red doublet is due to the Ag(III)-oxide, there should be satellites present in the spectra - according to the work.[34]

It can be also noticed that the spectrum recorded for the 30% oxygen fraction has some extra intensity on the lower-energy side of the Ag 3d 5/2 metallic peak, the intensity not explained by the suggested fitting. As discussed above, the reported in several publications Ag(I) and (III) oxide responses are on the lower-energy side of the metallic doublet. It is, however, more probable that the extra intensity in our case is due to the imperfection in the fitting of the background which was very difficult to define in the low-intensity spectra. This consideration is supported by the analysis of the spectrum for the 20% oxygen fraction, where there is nothing below the metallic Ag 3d 5/2 peak, while the intensity above the metallic doublet is very similar in both spectra – for 20% and 30% oxygen. It would be inconsistent to assume in the 30%-spectrum a sudden appearance of a principally different feature at lower energy, while the rest of the two spectra and the experimental conditions used to record them are rather similar.

Summarizing, one should underline one more time the necessity for further studies.

Conclusions and Outlook

The present Master project occupied an academic year and included the commissioning of new experimental equipment and performing experiments at the FlexPes beamline in the synchrotron facility MAX IV in Lund. The necessary prerequisite for interpreting the experimental results has been to master the photoelectron spectroscopy technique- the main experimental method at the FlexPES beamline. In the current work, two separate experiment series have been carried out using a water-cluster source and a metal-cluster source. Both setups were newly assembled at MAX-IV with my participation, and the experiments performed were their first test at real conditions.

The water clusters of two distinctly different sizes were produced and studied in a beam: of sizes $\approx$1000 and $\approx$3000 atoms per cluster. The goal of the studies has been to relate the intensity of the primary electrons, produced inside the clusters as the result of photoionization by x-ray radiation, to the intensity of the so-called secondary electrons, "kicked out" from water clusters by the primary electrons on their way through the cluster. For that task, the beam of water clusters was exposed to the synchrotron radiation provided by the FlexPES beamline at the 1.5 GeV ring of MAX-IV Laboratory. Photoelectron spectroscopy with the Scienta R4000 analyzer was used to detect the primary and secondary electrons and to quantify their flux. The measurements were performed at different photon energies in the range from 40 to 250eV so that the primary electrons were provided with different kinetic energies. The increase of the primary electrons' kinetic energy led to a stronger than linear rise of the secondary electron intensity. This result confirms the assumption of the possible important role of the secondary electrons in radiotherapy of biological tissue tumors, the assumption which motivated this study. In the second series of experiments silver and silver-oxide clusters were produced in a beam by a dedicated setup attached to the FlexPES beamline endstation. Photo-electron spectroscopy using the Scienta R4000 analyzer allowed us to detect for the first time Ag 3d core-level spectra for free metallic-silver and silver-oxide clusters. The core-level spectra can provide important information on the two possible silver-oxidation states in the particles, and on the spectroscopic signature of such states' creation. The concept of the so-called oxide shift – the difference between the metallic and oxidized silver spectral responses has been used for that. From the experiments carried out, it follows with a large probability that the oxide shifts are positive and have a value of around or more than 2 eV. This is in contrast to the previous picture in which the shifts are negative and are below 1 eV for both oxidation states of silver. Additional support for the interpretation suggested in the present work is the observation of extra intensity in the Ag 3d spectra of the oxides, which can be assigned to the so-called satellite lines predicted to appear for the higher oxidation state. However, more studies are necessary for providing stronger statistical support for such conclusions.

Closing Statement

"By better understanding how things work at the microscopic level we can design a better macroscopic future."

References

[1] P. Jena and J. A. W. Castleman, Nanoclusters : a bridge across disciplines (Elsevier, 2010).

[2] A. W. Castleman and K. H. Bowen, "Clusters: structure, energetics, and dynamics of intermediate states of matter", The Journal of Physical Chemistry **100**, 12911–12944 (1996).

[3] J. George A and M. J. Minch, "An introduction to hydrogen bonding (jeffrey, george a.)", Journal of Chemical Education **76**, 759 (1999).

[4] C. Bobbert, S. Schütte, C. Steinbach, and U. Buck, "Fragmentation and reliable size distributions of large ammonia and water clusters", The European Physical Journal D **19**, 183–192 (2002).

[5] Pacchioni and Gianfranco, Cluster models for surface and bulk phenomena, edited by G. Pacchioni, P. S. Bagus, and F. Parmigiani (Springer US, 1992).

[6] , Hypothetical (h2o)100 icosahedral water cluster, created using jmol, taken from: http://www.lsbu.ac.uk/water/escs2.html, https://commons.wikimedia.org/wiki /File: Iscosahedralwatercluster100.png.

[7] R. E. Benfield, "Mean coordination numbers and the non-metal–metal transition in clusters", J. Chem. Soc., Faraday Trans. **88**, 1107–1110 (1992).

[8] K. D. Sattler, Handbook of nanophysics, Vol. Volume 2. Handbook of Nanophysics - Clusters and Fullerenes (Crc Press, 2011), Chapter 7.

[9] C. B. 3. CCoil, https://upload.wikimedia.org/wikipedia/commons/b/b4/Silver %28I%29-oxide-unit-cell-3D-SF.png, Dec. 2020.

[10] Y. Dai, B. B. Huang, R. Long, and L. Yu, "Theoretical study of differences between surface and bulk electronic states in cu clusters", (2007).

[11] R. M. Shields, B. Temelso, K. A. Archer, T. E. Morrell, and G. C. Shields, "Accurate predictions of water cluster formation, (h2o)n=2-10", The Journal of Physical Chemistry A **114**, 11725–11737 (2010).

[12] F. N. Keutsch and R. J. Saykally, "Water clusters: untangling the mysteries of the liquid, one molecule at a time", Proceedings of the National Academy of Sciences **98**, 10533–10540 (2001).

[13] M. Tchaplyguine, S. Peredkov, H. Svensson, J. Schulz, G. Öhrwall, M. Lundwall, T. Rander, A. Lindblad, H. Bergersen, S. Svensson, M. Gisselbrecht, S. L. Sorensen, L. Gridneva, N. Mårtensson, and O. Björneholm, "Magnetron-based source of neutral metal vapors for photoelectron spectroscopy", Review of Scientific Instruments **77**, 033106 (2006).

[14] B. Chapman, Glow discharge processes: sputtering and plasma etching (Wiley, Sept. 1980).

[15] L. Holland, Vacuum deposition of thin films (London Chapman and Hall, 1970).

[16] J. F. Moulder, Handbook of x-ray photoelectron spectroscopy: a reference book of standard spectra for identification and interpretation of xps data (Physical Electronics Division, Perkin-Elmer Corporation, 1992).

[17] D. M. Wood, "Classical size dependence of the work function of small metallic spheres", Physical Review Letters **46**, 749–749 (1981).

[18] B. v. Issendorff and O. Cheshnovsky, "Metal to insulator transitions in clusters", Annual Review of Physical Chemistry **56**, 549–580 (2005).

[19] J. Urban and B. Tesche, "Size determination of silver clusters by time-of-flight mass spectroscopy and electron microscopy", Thin Solid Films **137**, 325–335 (1986).

[20] K. Wegner, P. Piseri, H. V. Tafreshi, and P. Milani, "Cluster beam deposition: a tool for nanoscale science and technology", Journal of Physics D: Applied Physics **39**, R439–R459 (2006).

[21] M. Inc, Meivac, 2.5 inch mak planar magnetron sputter source – l400a01, Meivac.com, 2020.

[22] S. B. Hagstrom, "Kai manne börje siegbahn", Physics Today **60**, 74–75 (2007).

[23] W. B. Peatman, Gratings, mirrors and slits: beamline design for soft x-ray synchrotron radiation sources (CRC Press, May 1997).

[24] H. Wabnitz, L. Bittner, A. R. B. de Castro, R. Döhrmann, P. Gürtler, T. Laarmann, W. Laasch, J. Schulz, A. Swiderski, K. von Haeften, T. Möller, B. Faatz, A. Fateev, J. Feldhaus, C. Gerth, U. Hahn, E. Saldin, E. Schneidmiller, K. Sytchev, K. Tiedtke, R. Treusch, and M. Yurkov, "Multiple ionization of atom clusters by intense soft x-rays from a free-electron laser", Nature **420**, 482–485 (2002).

[25] A. KOKALJ, P. GAVA, S. DEGIRONCOLI, and S. BARONI, "What determines the catalyst's selectivity in the ethylene epoxidation reaction", Journal of Catalysis **254**, 304–309 (2008).

[26] H. Haberland, M. Mall, M. Moseler, Y. Qiang, T. Reiners, and Y. Thurner, "Filling of micron-sized contact holes with copper by energetic cluster impact", Journal of Vacuum Science & Technology A: Vacuum, Surfaces, and Films **12**, 2925–2930 (1994).

[27] N. N. Greenwood and A. Earnshaw, Chemistry of the elements (Elsevier Butterworth-Heinemann, , Cop, 2016).

[28] M. Bielmann, P. Schwaller, P. Ruffieux, O. Gröning, L. Schlapbach, and P. Gröning, "Ago investigated by photoelectron spectroscopy:evidence for mixed valence", Physical Review B **65**, 10.1103/physrevb.65.235431 (2002).

[29] L. S. Kibis, V. I. Avdeev, S. V. Koscheev, and A. I. Boronin, "Oxygen species on the silver surface oxidized by mw-discharge", Surface Science **604**, 1185–1192 (2010).

[30] M. Tchaplyguine, C. Zhang, T. Andersson, and O. Björneholm, "Tuning the oxidation degree in sub-10 nm silver-oxide nanoparticles: from ag2o monoxide to ago (x> 1) superoxide", Chemical Physics Letters **600**, 96–102 (2014).

[31] L. H. Tjeng, M. B. J. Meinders, J. van Elp, J. Ghijsen, G. A. Sawatzky, and R. L. Johnson, "Electronic structure ofag2o", Physical Review B **41**, 3190–3199 (1990).

[32] G. B. Hoflund, J. F. Weaver, and W. S. Epling, "Ag2o xps spectra", Surface Science Spectra **3**, 157–162 (1994).

[33] D. Lützenkirchen-Hecht, "Anodic silver oxide (ago) layers by xps", Surface Science Spectra **18**, 102–109 (2011).

³⁴T. C. Kaspar, T. Droubay, S. A. Chambers, and P. S. Bagus, "Spectroscopic evidence for ag(iii) in highly oxidized silver films by x-ray photoelectron spectroscopy", The Journal of Physical Chemistry C **114**, 21562–21571 (2010).

³⁵G. B. Hoflund, J. F. Weaver, and W. S. Epling, "Ag foil by xps", Surface Science Spectra **3**, 151–156 (1994).

³⁶G. B. Hoflund, J. F. Weaver, and W. S. Epling, "Ago xps spectra", Surface Science Spectra **3**, 163–168 (1994).

³⁷D. Lützenkirchen-Hecht, "Electrochemically grown silver oxide (ag2o) by xps", Surface Science Spectra **18**, 96–101 (2011).

³⁸C. Wright, C. Zhang, M.-H. Mikkelä, E. Mårsell, A. Mikkelsen, S. Sorensen, O. Björneholm, and M. Tchaplyguine, "Tin oxides: insights into chemical states from a nanoparticle study", The Journal of Physical Chemistry C **121**, 19414–19419 (2017).

³⁹F. R. Elder, A. M. Gurewitsch, R. V. Langmuir, and H. C. Pollock, "Radiation from electrons in a synchrotron", Physical Review **71**, 829–830 (1947).

⁴⁰V. Schmidt, "Photoionization of atoms using synchrotron radiation", Reports on Progress in Physics **55**, 1483–1659 (1992).

⁴¹, Beamline map, https://www.maxiv.lu.se, Nov. 2020.

⁴²A. Kivimäki, K. Maier, U. Hergenhahn, M. N. Piancastelli, B. Kempgens, A. Rüdel, and A. M. Bradshaw, "Subnatural linewidths in core level excitation spectra", Physical Review Letters **81**, 301–304 (1998).

⁴³M. Bässler, A. Ausmees, M. Jurvansuu, R. Feifel, J.-O. Forsell, P. de Tarso Fonseca, A. Kivimäki, S. Sundin, S. Sorensen, R. Nyholm, O. Björneholm, S. Aksela, and S. Svensson, "Beam line i411 at max ii—performance and first results", Nuclear Instruments and Methods in Physics Research Section A: Accelerators, Spectrometers, Detectors and Associated Equipment **469**, 382–393 (2001).

⁴⁴M. Mucke, M. Braune, S. Barth, M. Förstel, T. Lischke, V. Ulrich, T. Arion, U. Becker, A. Bradshaw, and U. Hergenhahn, "A hitherto unrecognized source of low-energy electrons in water", Nature Physics **6**, 143–146 (2010).

⁴⁵Thermopedia, Steam tables, thermopedia.com, Dec. 2020.

⁴⁶G. Ohrwall, R. F. Fink, M. Tchaplyguine, L. Ojamae, M. Lundwall, R. R. T. Marinho, A. d. Brito, S. R. Sörensen, M. Gisselbrecht, R. Feifel, T. Rander, A. Lindblad, J. Schulz, L. J. Saethre, N. Mårtensson, S. Svensson, and O. Bjorneholm, "The electronic structure of free water clusters probed by auger electron spectroscopy", Journal of Chemical Physics **123**, 054310 (2005).

⁴⁷C. Zhang, T. Andersson, S. Svensson, O. Björneholm, and M. Tchaplyguine, "Core-shell structure in self-assembled lead/lead-oxide nanoclusters revealed by photoelectron spectroscopy", Physical Review B **87**, 10.1103/physrevb.87.035402 (2013).

⁴⁸N. I. of Standards and Technology, Energy levels of singly ionized silver ag(ii), physics.nist.gov, Oct. 2020.

⁴⁹M. Tchaplyguine, M.-H. Mikkelä, C. Zhang, T. Andersson, and O. Björneholm, "Gold oxide nanoparticles with variable gold oxidation state", The Journal of Physical Chemistry C **119**, 8937–8943 (2015).

[50]P. M. Sherwood, "Rapid evaluation of the voigt function and its use for interpreting x-ray photoelectron spectroscopic data", Surface and Interface Analysis **51**, 254–274 (2018).

[51]G. Öhrwall, M. Tchaplyguine, M. Gisselbrecht, M. Lundwall, R. Feifel, T. Rander, J. Schulz, R. R. T. Marinho, A. Lindgren, S. L. Sorensen, S. Svensson, and O. Björneholm, "Observation of elastic scattering effects on photoelectron angular distributions in free xe clusters", Journal of Physics B: Atomic, Molecular and Optical Physics **36**, 3937–3949 (2003).

[52]J. Yeh and I. Lindau, "Atomic subshell photoionization cross sections and asymmetry parameters: $1 \leq z \leq 103$", Atomic Data and Nuclear Data Tables **32**, 1–155 (1985).

[53]P. Vacuum, Vacuum technology and vacuum pumps from the leader, Pfeiffer-vacuum.com, 2019.

Bibliography

Books

- P. Jena and Jr A Welford Castleman, Nanoclusters: A Bridge across Disciplines (Elsevier, Amsterdam, 2010).

- Editors: Pacchioni, Gianfranco, Bagus, Paul S., Parmigiani, Fulvio (Eds.), Cluster Models for Surface and Bulk Phenomena (Springer US, 1992).

- P. Willmott and J. Wiley, An Introduction to Synchrotron Radiation: Techniques and Applications (Hoboken, Nj; Chichester, West Sussex Wiley, 2019).

- P.P. Wegener, Molecular Beams and Low Density Gasdynamics (Dekker, 1974).

- J H De Leeuw, Rarefied Gas Dynamics (Academic Pr., -6, N.Y., 1965).

- A.C. Thompson, L. Berkeley, and L. Berkeley, X-Ray Data Booklet (Lawrence Berkeley National Laboratory, University Of California, Berkeley, Calif., 2001).

- S. Werin, Accelerator Technique - (Copyright) Sverker Werin, Max-Lab 2006, 2.5 Edition (MAX-lab/Lund University, 2003).

- P. Willmott and J. Wiley, An Introduction to Synchrotron Radiation: Techniques and Applications (Hoboken, Nj; Chichester, West Sussex Wiley, 2019).

Articles

- A.W. Castleman and K.H. Bowen, The Journal of Physical Chemistry 100, 12911 (1996).

- R.M. Shields, B. Temelso, K.A. Archer, T.E. Morrell, and G.C. Shields, The Journal of Physical Chemistry A 114, 11725 (2010).

- F.N. Keutsch and R.J. Saykally, Proceedings of the National Academy of Sciences 98, 10533 (2001).

- J.C. Walton, Molecules: A Journal of Synthetic Chemistry and Natural Product Chemistry 23, (2018).

- V. Schmidt, Reports on Progress in Physics 55, 1483 (1992).

- J. Braun, A. Baidins, and R. Marganski, Progress in Organic Coatings 20, 105 (1992).

- T. Jahnke, Journal of Physics B: Atomic, Molecular and Optical Physics 48, 082001 (2015).

- J.J. Yeh and I. Lindau, Atomic Data and Nuclear Data Tables 32, 1 (1985).

- C. Zhang, T. Andersson, M.-H. Mikkelä, E. Mårsell, O. Björneholm, X. Xu, M. Tchaplyguine, and Z. Liu, The Journal of Chemical Physics 141, 084302 (2014).

- C. Zhang, T. Andersson, O. Björneholm, X. Xu, M. Tchaplyguine, and Z. Liu, The Journal of Physical Chemistry C 117, 14390 (2013).

- C. Zhang, T. Andersson, S. Svensson, O. Björneholm, and M. Tchaplyguine, Physical Review B 87, (2013).

- M.A. Hoffmann, G. Wrigge, and B. v. Issendorff, Physical Review B 66, (2002).

- H. Häkkinen, M. Moseler, O. Kostko, N. Morgner, M.A. Hoffmann, and B. v. Issendorff, Physical Review Letters 93, (2004).

- N. Britun, M. Palmucci, S. Konstantinidis, and R. Snyders, Journal of Applied Physics 117, 163302 (2015).

- C. Langlois, Z.L. Li, J. Yuan, D. Alloyeau, J. Nelayah, D. Bochicchio, R. Ferrando, and C. Ricolleau, Nanoscale 4, 3381 (2012).

- S. Piccinin, S. Zafeiratos, C. Stampfl, T.W. Hansen, M. Hävecker, D. Teschner, V.I. Bukhtiyarov, F. Girgsdies, A. Knop-Gericke, R. Schlögl, and M. Scheffler, Physical Review Letters 104, (2010).

- M.O. Ozbek, I. Onal, and R.A. van Santen, Journal of Catalysis 284, 230 (2011).

- M. Tchaplyguine, S. Peredkov, A. Rosso, J. Schulz, G. Öhrwall, M. Lundwall, T. Rander, A. Lindblad, H. Bergersen, W. Pokapanich, S. Svensson, S.L. Sorensen, N. Mårtensson, and O. Björneholm, The European Physical Journal D 45, 295 (2007).

- W. Klemm, Angewandte Chemie International Edition in English 2, 332 (1963).

- T. Lünskens, P. Heister, M. Thämer, C.A. Walenta, A. Kartouzian, and U. Heiz, Physical Chemistry Chemical Physics 17, 17541 (2015).

- J. Vollet, J.R. Hartig, and H. Schnöckel, Angewandte Chemie International Edition 43, 3186 (2004).

- F.R. Elder, A.M. Gurewitsch, R.V. Langmuir, and H.C. Pollock, Physical Review 71, 829 (1947).

- A.M. Tokmachev, A.L. Tchougréeff, and R. Dronskowski, ChemPhysChem 11, 384 (2010).

- J. JANKOWIAK and M. BARTEAU, Journal of Catalysis 236, 366 (2005).

- J.G. Kay, Science 144, 703 (1964).

- H. EMELEUS, Endeavour 35, 45 (1976).

Reports

- A. Fielicke, Methods to Produce and Study Clusters (n.d.).

Websites

- M. Inc, Meivac.com (2020).
- Pfeiffer Vacuum, Pfeiffer-Vacuum.com (2019).
- Thermo Fischer Scientific, Xpssimplified.com (n.d.).

List of Figures

List of Acronyms

XPS   X-ray PhotoElectron Spectroscopy

SR   Synchrotron Radiation,

PES   PhotoElectron Spectroscopy

TEM   Transmission Electron Microscopy

ESCA   Electron Spectroscopy for Chemical Analysis

VUV   Vacuum Ultra Violet

UPS   Ultraviolet Photoelectron Spectroscopy

FEL   Free Electron Laser

UHV   Ultra High Vacuum

PLC   Programmable Logic Control

Notations

The next list describes several symbols that will were used in this thesis

Δ Enthalpy

Γ^* Reduced Scaling Parameter

ρ Density

c Speed of light in a vacuum inertial frame

d Nozzle Orifice Diameter

d^q Empirically Adjusted Nozzle Orifice Diameter

h Planck constant

n_o Concentration of Molecules in Vapour

r_{ch} The Ratio of Mass m to Density ρ and Enthalpy Δ

T_0 Nozzle Temperature

q,D,α Free Parameters for Water

Greek Letters and their meaning

Character	Name	Character	Name
α	alpha *AL-fuh*	ν	nu *NEW*
β	beta *BAY-tuh*	ξ, Ξ	xi *KSIGH*
γ, Γ	gamma *GAM-muh*	o	omicron *OM-uh-CRON*
δ, Δ	delta *DEL-tuh*	π, Π	pi *PIE*
ϵ	epsilon *EP-suh-lon*	ρ	rho *ROW*
ζ	zeta *ZAY-tuh*	σ, Σ	sigma *SIG-muh*
η	eta *AY-tuh*	τ	tau *TOW (as in cow)*
θ, Θ	theta *THAY-tuh*	υ, Υ	upsilon *OOP-suh-LON*
ι	iota *eye-OH-tuh*	ϕ, Φ	phi *FEE, or FI (as in hi)*
κ	kappa *KAP-uh*	χ	chi *KI (as in hi)*
λ, Λ	lambda *LAM-duh*	ψ, Ψ	psi *SIGH, or PSIGH*
μ	mu *MEW*	ω, Ω	omega *oh-MAY-guh*

Table 5.2: *Greek letters*

Appendix

The process for deriving the mean cluster size:

According to Bobbert et al. [4] the scaling parameter Γ can be calculated using the relation:

$$\Gamma = n_0 d^q T_o^{sq-\frac{f}{2}} \quad for \quad 0 < q < 1 \tag{5.2}$$

To do this, we need to know the parameters n_0, d^q, and T_0. The power "q" of the diameter d is an empirical parameter found in Bobbert[4]. A nozzle is often not just a hole in a plane surface, but has a shape of a diverging towards a vacuum cone of a narrow opening angle. As was should be discussed in this Thesis, the nozzle used in our experiment was of such a conical shape with the orifice diameter of 150 micrometres and the half opening angle of 10 degrees. To use formula 5.2 we must find the so-called equivalent diameter (which takes into account the conical shape and the angle) for our nozzle, and which is given by the relationship:

$$D_{eq} = \frac{G(f)d}{(tan(a))} \tag{5.3}$$

With G(f) defined as a function of "f" which is the number of energetically active degrees of freedom, and which also defines "s" in expression 5.2 above: s= (f-2)/4. According to Bobbert et al. G(f) is defined as:

$$G(f) = 0.5 * (f+1)^{-\frac{f+1}{4}} * A^{\frac{f}{2}} \tag{5.4}$$

Here we have to be careful because three types of "alpha" are used in the work by Bobbert et al. The angle of the nozzle is denoted by "a" which is 10 degrees, the parameter a which is $a = q - 3 = 2,336$ (with q being an empirical parameter) and the "alpha" that is a tabulated parameter for each specific type of gas/vapour (for water vapour "alpha" was 1,886). For our application the constant $A = 3,83$ for a three-dimensional axisymmetric flow. [4] To calculate the reduced scaling parameter Γ^* we need another parameter called K_{ch} which is defined as $K_{ch} = rq - 3 * T_a$ and for water we used $r_{ch} = 3,19 * A$ and $T_{ch} = 5684K$. where r_{ch} is the ratio of mass m to density ρ and enthalpy Δ given by:

$$r_{ch} = (\frac{m}{\rho})^{\frac{1}{3}} \quad and \tag{5.5}$$

$$kT_{ch} = \Delta h \tag{5.6}$$

Once we have all these, we calculate Γ^* by using :
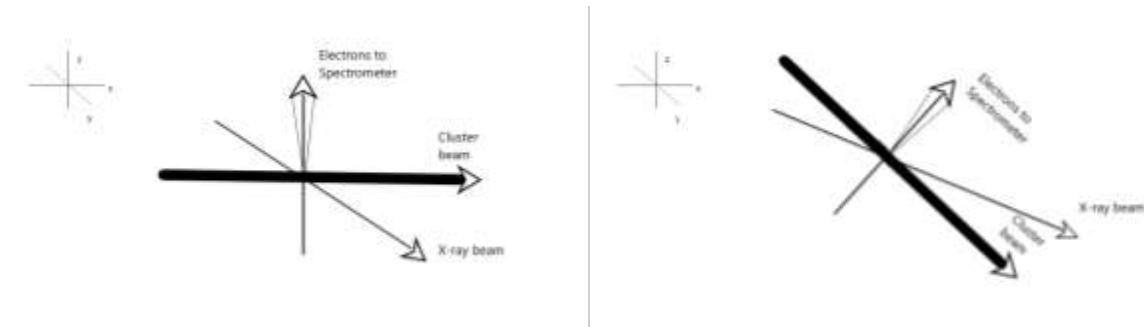
$$\Gamma^* = \frac{\Gamma}{K_{ch}} \tag{5.7}$$

And then in turn use a power law to find the mean cluster size:

$$< n >= D(\frac{\Gamma^*}{1000})^{\alpha} \tag{5.8}$$

xviii

With the free parameters q, D as well as α taken from tables for water to be: $q = 0,634, q - 3 = -2,336, D = 11,60, a = 1,886$.

The magic angle description:

In Figure 5.13 we visualise the described geometry, with the cluster beam included.

(a) Our schematic experimental configuration: *(b) Our schematic experimental configuration:*
The normal intersection of the x-ray beam with The adjusted intersection of the x-ray beam with
the cluster path and the ejection of photoelectron the cluster path and the ejection of photoelectron
in a non-specific angle *in the magic angle*

Figure 5.13: *On figure 5.13a we can see the intersection of the three axes we described and on figure 5.13b the same intersection tilted to have the magic angle configuration for the spectrometer*

The angle of $\theta = 54,7°$ appears for atomic ionisation in the so-called dipole approximation for the ionization process.

The theory of ionization deals with the so-called differential cross-section $\delta\sigma/\delta\Omega$ - describing the probability to emit electrons into an infinitely small solid angle $\delta\Omega$. This differential cross-section is given in by the following formula by V.Schmidt [40]:

$$\frac{\delta\sigma}{\delta\Omega} = \frac{\sigma}{4\pi}(1 + \frac{\beta}{4}(3\cos 2\theta + 1)) \tag{5.9}$$

where σ is the total cross-section (integrated over the solid angle 4π), β is the anisotropy parameter of the angular distribution, and θ is the angle between the polarisation vector and the electron ejection axis. As mentioned above, this equation applies to atomic photo-ionization, but it can be used as a guideline for more complex systems as for water clusters, considering that we deal with randomly oriented and not fixed in space objects.[51]

As can be seen from the equation, for the magic angle the expression in the internal brackets becomes equal to zero what elements the $\delta\sigma/\delta\Omega$ dependence on the anisotropy:

$$\frac{\delta\sigma}{\delta\Omega} = \frac{\sigma}{4\pi} \quad with \quad \frac{\delta\sigma}{\delta\Omega} > 0 \quad , \quad \sigma > 0 \tag{5.10}$$

The differential cross-section $\delta\sigma/\delta\Omega$ remains dependent only on the total ionization cross-section σ. Since the differential cross-section can be larger or equal to zero it means that there are certain demands on $\beta : -1 \leq \beta \leq 2$ and that positive values give

the differential cross-section larger in the direction parallel to the polarisation of the incident light while negative values give a direction perpendicular to the polarisation field.

$$(1 + \frac{\beta}{4}(3\cos 2\theta + 1) > 0$$
$$\beta > -\frac{4}{3\cos 2\theta + 1} \quad (-1 \leq \cos 2\theta \leq 1)$$
$$\beta \leq 2 \quad \beta \geq -1$$

There is a database of cross-sections calculated by Yeh & Lindau [52] (which is one of the most cited publications in the world). It provides data for the cross-section values of almost all elements of the Periodic Table. There the cross-sections are given as a function of photon energy for each state of each element
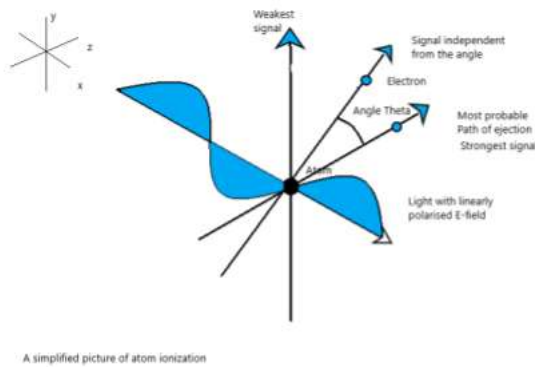
Figure 5.14: *A simplified sketch showing different critical paths of the elected electrons. The path along the magic angle depends only on the total ionization cross-section (in the dipole approximation and for separate atoms)*

Notes on the peripheral equipment of the beamline :

The FlexPES beamline and its B-endstation are sophisticated technical assemblies incorporating mechanical, electrical, electronics, computer, network, automation, and other components. A lot of "peripheral" systems and equipment has to be implemented for the users to be able to perform their experiments at the beamline and endstation. The beamline and endstation demand vacuum pumping, cooling, heating, temperature monitoring, facilities for cleaning of parts, and assembling. For the purpose of pumping, the beamline is equipped with several so-called dry fore-vaccum pumps -a significant improvement relative to the previously implemented (at the old MAX-lab) oil-using fore-vacuum pumps that contaminated setups with their oil. The pumps were developed by Adixen company, now a part of Pfeiffer Vacuum [53]. They provide the baseline pressure of low vacuum in the range of a 10^{-3} mbar that is needed for the so-called turbo-pumps (described below) -also by Pfeiffer Vacuum- for pumping towards high vacuum conditions.

Although the dry fore-vacuum pump have this advantage of being non -contaminating, they have the disadvantage of being very noisy and producing a lot of heat, so at the beamline they are installed in special cabinets that are cooled and sound-isolating. The fore-vacuum pumps are connected with 40-mm diameter tubes

to the inputs of turbo pumps, via the so-called KF40 flange connections. There are eight fore-vacuum pumps serving the end-station and two sections of the beamline. The Pfeiffer turbo pumps are able to reach pressures of around 10-9 mbar, considered as high vacuum. Most turbo pumps at the beamline have around 300 litres/second pumping capacity, with their turbine having a rotation speed of 60000 rpms when working at full speed. There are models which use magnetic-levitation bearings for holding the turbine. These pumps can take high gas loads and avoid otherwise common overheating. Two of such pumps were used for the water-cluster source, and one pump for the metal-cluster source. As a rule, the turbo pumps need to be connected to water for cooling. The controllers for the turbo-pumps of the beamline and of the endstation are installed in another cabinet, and users can turn them on and off when necessary. Both the fore-vacuum pumps and the turbo pumps are integrated in an automated control system of the beamline – the so-called Programmable Logic Control (PLC). There are additional ultra high vacuum pumps Ultra High Vacuum (UHV) installed at certain sections of the beamline—the so-called ion pumps that make that final step to pressures of 10-10 mbar. Such pumps are used for the vacuum chambers where the beamline's optical elements are placed, and where the photon beam is shaped by various slits and baffles. Such ultra high vacuum is not used in the endstation of branch B, as it is a process that requires several steps, a long time and baking of the stainless steel chambers. In view of the typical experiments at branch B with the high gas input, the UHV vacuum is not necessary.

The vacuum level itself is measured with gauges. There are so-called Cold Cathode gauges and the Pirani gauges, each operating in an appropriate vacuum range. The Cold Cathode Gauge is meant for vacuum better than $5 * 10^{-3}$ mbar up to 10^{-10} mbar and its working principle is to measure the current in a plasma it creates with an electrical discharge-similar to how a magnetron creates plasma. The Pirani gauge has a working range from atmospheric to $5 * 10^{-4}$ and its working principle is to use a thermal conducting element to measure the different conductivity of gases depending on their concentration. They are both used independently or combined as the so-called Full Range Gauge. Together they cover the whole vacuum range, from atmospheric to ultra high. There are many gauges installed at the beamline to independently control vacuum at the beamline different sections. All gauges are also integrated into the automated control system of the beamline. In a complicated way, this control system provides information to the program steering different components of the beamline. The results of the vacuum measurements by the gauges are transferred to the graphical user-interface of the steering program.

Lastly, for different types of cooling, there are centralized cooled water lines connected to various elements of the beamline, like for example, the turbo pumps or mirrors, but also available for users to use for their pumps and their setups. Apart from the centralized water-cooling system, there is a small portable cooling station for cooling separate user parts. There is also the option of liquid nitrogen use for cryogenic cooling of the parts of the user equipment and the sample. Although there are no dedicated lines for gas supply apart from a line of compressed air at this beamline, it can be the case in the future. The gases are provided as needed in pressurised bottles. A gas supply system is under construction at FlexPES. The electric, electronic, network, automation, and control equipment is placed in multiple dedicated racks. There are also two dedicated cranes for lifting heavy equipment.

Log book examples used during experiments:

Figure 5.15: *Log book example used during experiments.*

Figure 5.16: *A quite afternoon at FlexPES - MAX IV*

X-ray Photoelectron Spectroscopy on Clusters: From Water Clusters to Metal & Metal-Oxide Nanoparticles

Clusters are particles consisting of several identical atoms or molecules bound together. Some clusters exist around us, like soot particles or tiny water droplets. Many other clusters can only be produced in a laboratory. There is an increasing interest in cluster research because of their growing range of applications, and because they can serve as models for macroscopic systems. In this work, the clusters contained a few thousand atoms or molecules and were studied at the MAX-IV synchrotron facility using spectroscopic techniques.

The first part of the thesis concerns water clusters. Energizing water clusters with radiation allows researchers to study problems connected to radiation therapy. In radiotherapy, it is believed that a special type of electrons that are produced when the water in biological tissue is targeted can play a role in destroying tumour cells. In the current study of water clusters, the production of these electrons is a model for the process, a model that can tell us how many of these electrons we can produce with what energy. The results of the experiments carried out in this work show a strong connection between these electrons that we call secondary electrons and their precursors, and a clear trend of how their production increases with the energy we apply. These results add to our understanding of the radiotherapy method.

The second part of the thesis is dedicated to producing and studying silver and oxidized silver nanoparticles. They can be used to model a part of a chemical reaction that usually takes place in chemical factories and it is called "ethylene epoxidation through catalytic production". This reaction is important because its product the main ingredient used for making detergents. The silver-oxide particles are used to make oxygen available for the oxidation of ethylene to happen. The problem is that silver 'oxides can be of different types, and there is little information on what and how much of each is ever there. By studying the silver-oxide particles with radiation, we can hope to identify what oxides are formed. The results we get can help researchers to distinguish and identify these silver oxides and improve this important catalytic process. I wrote this thesis to showcase my effort, our results, and hopefully to actively contribute to these subjects. My hope is that this work will add to current literature and also inspire other people to see the usefulness and value of this research.

■